https://ntrs.nasa.gov/search.jsp?R=19850009402 2020-03-20T20:32:19+00:00Z

General Disclaimer

One or more of the Following Statements may affect this Document

- This document has been reproduced from the best copy furnished by the organizational source. It is being released in the interest of making available as much information as possible.

- This document may contain data, which exceeds the sheet parameters. It was furnished in this condition by the organizational source and is the best copy available.

- This document may contain tone-on-tone or color graphs, charts and/or pictures, which have been reproduced in black and white.

- This document is paginated as submitted by the original source.

- Portions of this document are not fully legible due to the historical nature of some of the material. However, it is the best reproduction available from the original submission.

Produced by the NASA Center for Aerospace Information (CASI)

Final Report: September 1, 1981 - April 30, 1983

Grant: NASA-NAG-1-204

Silicon Superlattices II: Si-Ge Heterostructures and MOS Systems

Principal Investigator: J. A. Moriarty†
Department of Electrical and Computer Engineering
University of Cincinnati, Cincinnati, OH 45221

NASA Technical Officer: R. L. Stermer
NASA-Langley Research Center, Hampton, VA 23665

†Present Address:

Lawrence Livermore National Laboratory
University of California
Livermore, CA 94550

(NASA-CR-174287) SILICON SUPERLATTICES. 2: Si-Ge HETEROSTRUCTURES AND MOS SYSTEMS Final Report, 1 Sep. 1981 - 30 Apr. 1983 (Cincinnati Univ.) 49 p HC A03/MF A01 CSCL 20L G3/76

N85-17711

Unclas 01341

I. INTRODUCTION

The device-application potential of ultrathin periodically-layered semiconductors, commonly known as superlattices, has attracted a great deal of recent attention, since the pioneering work of Esaki and collaborators[1,2] in the early 1970's. In constrast to the mainstream of research on III-V materials, our interest in semiconductor superlattices has focused on the possibilities offered by creating such structures in silicon, still the most technologically important electronic material. In this report we summarize the second phase of a comprehensive theoretical study of silicon-superlattice electronic structure and its implications for enhanced carrier mobilities in such systems. The first, preliminary phase of this work was performed under NASA grant NAG-1-33 and included detailed studies of hypothetical one- and two-dimensional systems, as well as the formulation of the basic three-dimensional model upon which the present investigation has focused.

Our efforts during the present grant period have been concentrated in five main areas:

(i) A highly-refined and intensive investigation of both the valence- and conduction-band-edge electronic structure of the thin-layer (< 11 A) silicon-superlattice systems, utilizing the methodology developed during the first phase of this work. The results of this study have been recently published.[3]

(ii) The development of a new theoretical method for extending our thin-layer calculations to layers of thicknesses > 11 A, where most potential experimental interest lies.

(iii) A corresponding intensive investigation of the electronic structure of thicker-layer (11-110 A) silicon superlattices.

(iv) Preliminary calculations of impurity-scattering-limited electron mobility in the thicker-layer superlattices.

(v) The selection and testing of an experimental method for producing the fine metal lines that would be required to produce an MOS superlattice.

In addition to the principal investigator, S. Krishnamurthy, as a graduate student in the Department of Physics, participated in all five of the above research areas. The work reported in areas (ii), (iii), and (iv) has comprized a major portion of his Ph.D. thesis[4] and will also be published.[5] Additional participatants in area (v) were Dr. K. P. Roenker, Assistant Professor of Electrical Engineering, and

E. Craig, graduate student in the Departmant of Electrical and Computer Engineering.

In Sec. II, the major theoretical considerations which have guided our work are reviewed. Then in Secs. III and IV, respectively, our electronic structure calculations covering areas (i), (ii), and (iii) and our mobility calculations covering area (iv) are presented and discussed. Finally, our efforts to experimentally produce the fine metal lines of area (v) are summarized in Sec. V. Concluding remarks are given in Sec. VI, while a bibliography of conference papers and journal publications resulting from this work are collected in Sec. VII.

II. GENERAL THEORETICAL CONSIDERATIONS

A. Possible physical structures

Within the confines of silicon materials technology (i.e., excluding III-V and II-VI materials), the number of possible superlattice structures is greatly limited. With regard to conventional layered structures, the Si-$Si_{1-x}Ge_x$ system is the prototype silicon superlattice. In addition to our theoretical work on this system, a preliminary experimental investigation of Si-$Si_{1-x}Ge_x$ superlattices has been made at Rockwell International.[6] Quite interestingly, their results showed evidence of enhanced transverse electron mobility even without deliberate modulation doping. This observation is actually in sharp constrast to the GaAs-$Ga_{1-x}Al_xAs$ system, in which the uniformly doped superlattice shows significantly decreased mobility below the bulk,[7] and strongly suggests that additional physical mechanisms are at work in Si-$Si_{1-x}Ge_x$. Our theoretical studies indeed suggest a second possible mechanism, one of quantum origin arising from the uniquely modified electronic structure in silicon-based superlattices. In particular, we find a reduced transverse conductivity effective mass associated with the superlattice band structure, as discussed in Sec. III below. It is unclear at this point, however, whether or not this effect is actually playing a role in the observed enhanced mobility. For one thing, the experimental program at Rockwell concentrated on generally thick-layer (> 300 A) systems, where such a quantum effect should be greatly diminished. Secondly, the Rockwell Si-$Si_{1-x}Ge_x$ superlattices have been grown with a chemical-vapor-deposition (CVD) technique in which the quality of the interfaces is not rigidly controlled. Possible interface strain fields and other nonuniformities cloud any straight-forward interpretation of their results in terms of our theoretical predictions. Attempts to grow better superlattices, utilizing the more-precise technique of molecular-beam-expitaxy (MBE)[2] and accomodating the lattice mismatch in a strained-layer structure,[8] have recently been undertaken at Bell Laboratories.[9]

Beyond the Si-$Si_{1-x}Ge_x$ system, silicon materials technology offers some other novel possibilities for superlattice structures. One is an MOS (metal-oxide-silicon) configuration with a grided metal electrode made up of fine parallel metal lines uniformly spaced on the oxide layer.[10] (See Fig. 1.) In this system, it is envisioned that an extra periodic electron potential could be extended into the silicon by holding alternate metal lines in the grid at different voltages. The primary technological challenge of creating such a system comes in producing a periodic metal electrode pattern of the ultrathin dimensions required (< 500 A line spacings and thicknesses). We have done some exploratory work in this direction, focusing on (i) existing techniques

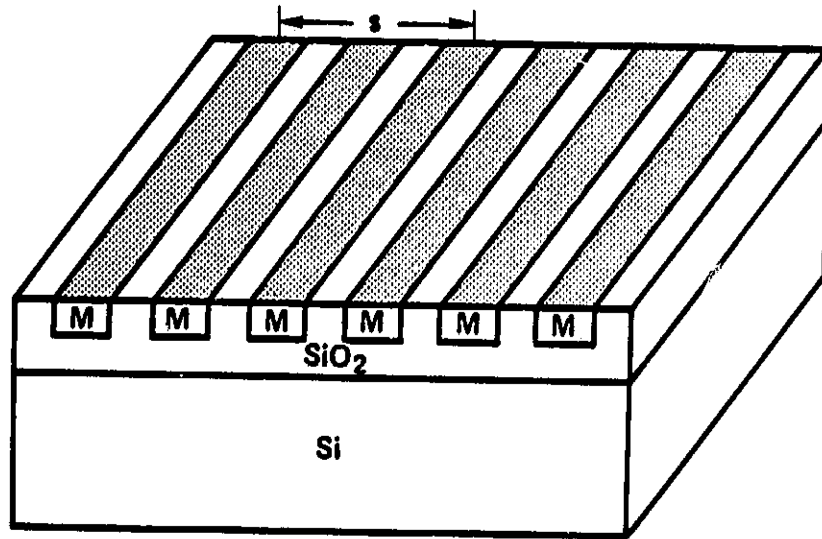

Fig. 1. Conceptual drawing of a possible MOS superlattice structure.

for producing fine metal lines of the required thickness and (ii) methods which could be tested with our laboratory facilities. After a literature search of current fine-line technology, we selected one promising method for laboratory testing. The results of this study are reported in Sec. V.

Another possible silicon superlattice structure could be one consisting of alternately *n*- and *p*-doped silicon layers. This type of system (the so-called *nipi* superlattice[11]) has been realized in GaAs with MBE,[12] and shows a number of interesting properties including a tunable band gap.[13] It turns out, however, that advantages such as modulation doping in enhancing carrier mobilities are lost in this type of superlattice.

B. Enhanced mobility

As in bulk semiconductors, there are three basic physical mechanisms which influence carrier mobilities in the ideal semiconductor superlattice: (i) impurity scattering, (ii) phonon scattering, and (iii) band edge electronic structure. The first, impurity scattering, is primarily dictated by the level and uniformity of doping. Its degrading effect on carrier mobility in the superlattice can be minimized by modulation doping. In this technique, only one of the two constituent layers in the superlattice is doped, and this is done in such a way as to segregate the added carriers from their parent ions. For example, if one dopes the constituent possessing the highest-lying bulk conduction-band edge (e.g., $Ga_{1-x}Al_xAs$) with shallow donors, the ionized donor electrons will migrate to the second constituent (e.g., GaAs) having the lower conduction-band edge. Application of a transverse electric field (i.e., one parallel to the layers) then allows the donor electrons to move in regions free of ionized impurity scattering centers, leading to enhanced transverse mobility. This effect is particularly striking at low temperatures,[7] where impurity scattering dominates other scattering mechanisms. Furthermore, the effect is not dependent on any quantum-mechanical coherence of the superlattice, but only on the heterostructure itself, and has now been observed in a single-period GaAs-$Ga_{1-x}Al_xAs$ heterostructure as well.[14]

For the Si-$Si_{1-x}Ge_x$ superlattice, modulation doping would appear to be less advantageous in principle because in this case it is the pure material constituent (Si) which posseses the higher-lying conduction-band edge, so that now the segregated donor electrons must move in the (disordered) alloy component ($Si_{1-x}Ge_x$). Thus reduced impurity scattering is traded for increased disorder scattering. This balance may nonetheless still be favorable, however, because the latter is not expected to be large, but this has not as yet been demonstrated experimentally.

The precise role of phonon scattering in altering superlattice mobility is also not well established at this point in time. Model calculation of the electron-phonon scattering rate in a layered superlattice simulating GaAs-$Ga_{1-x}Al_xAs$ suggests, in fact, that this rate should actually be enhanced rather than diminished.[15] The calculation assumes among other things, however, that both the phonons and the electronic band structure are unaltered in the superlattice, which is, generally speaking, not the case.

Carrier mobilities are also directly affected by the electronic structure of the material in which the carriers move. Of course, part of this dependence is already implicit in the impurity and phonon scattering rates, but we know from simple treatments of bulk semiconductors that a major effect of the band structure ultimately comes in the form of a multiplicative factor involving the conductivity effective mass m_c^*. Ideally, for ionized impurity scattering the mobility varies as $(m_c^*)^{-1/2}$ and for acoustic phonon scattering as $(m_c^*)^{-5/2}$. In the limit of a three-dimensional quantum-mechanically coherent superlattice, where carrier mean-free paths are long compared to the superlattice period s and the band structure is well defined, one expects similar premiums on effective mass, with m_c^* for the bulk replaced by an appropriate value for the superlattice. In silicon superlattices, this should be the case when $s \ll 1000$ A at room temperature or $s \ll 4000$ A at liquid nitrogen temperature.

Interestingly, one can make a number of general statements about the expected behavior of effective masses in the superlattice prior to doing detailed calculations. First, the usual isotropic conductivity in bulk diamond or zincblende crystals becomes anisotropic in the superlattice with distinct values parallel (i.e., transverse) and perpendicular (i.e., longitudinal) to the layers of the superlattice. A scalar conductivity effective mass in the bulk thus becomes a conductivity effective-mass tensor in the superlattice, involving both transverse and longitudinal masses, say, m_{hT}^* and m_{hL}^* for holes and m_{eT}^* and m_{eL}^* for electrons. As in the bulk, band edges in the superlattice occur along symmetry directions, and the electronic structure in the vicinity of each edge can be described in terms of transverse and longitudinal band masses, say, m_{hl}^* and m_{ht}^* for the valence band and m_{el}^* and m_{et}^* for the conduction band. (Here, as in customary bulk descriptions, longitudinal l refers to the direction of the symmetry axis and transverse t to the plane perpendicular to that axis.) In the usual case, where there is a simple one-to-one correspondence of the band edge in the superlattice with the band edge in the bulk, it is also useful to relate these latter masses to their counterparts in the bulk. For example, for the heavy-hole valence band with a band edge at the center of the Brillouin zone ($\underline{k} = 0$, the Γ point), one can write

$$m^*_{hl} = \alpha_l \; m^*_{hh} \tag{1}$$

and

$$m^*_{ht} = \alpha_t \; m^*_{hh} \; , \tag{2}$$

where m^*_{hh} is the bulk heavy-hole mass and α_l and α_t are enhancement or reduction factors which give the relative hole masses in the superlattice. Furthermore, in this case

$$m^*_{hL} = m^*_{hl} \tag{3}$$

and

$$m^*_{hT} = m^*_{ht} \; . \tag{4}$$

Similarly, for a single conduction band edge (not necessarily at $\underline{k} = 0$),

$$m^*_{el} = \beta_l \; m^*_l \tag{5}$$

$$m^*_{et} = \beta_t \; m^*_t \; , \tag{6}$$

where m^*_l and m^*_t are bulk masses and β_l and β_t are relative electron-mass factors. If the conduction band edge is also at $\underline{k} = 0$ (i.e., a direct-gap material), then $m^*_l = m^*_t$ and also $m^*_{eL} = m^*_{el}$ and $m^*_{eT} = m^*_{et}$. The more important case for our purposes is that of a silicon-like band structure with multiple equivalent band edges centered out along the <100> axes near the X-point zone boundaries. Then m^*_{eT} and m^*_{eL} are weighted averages of m^*_{et} and m^*_{el}. In the bulk, or course, there are six equivalent, effectively degenerate, minima with $m^*_c = m^*_{eT} = m^*_{eL}$ and

$$m^*_c = \frac{3}{[(1/m^*_l)+(2/m^*_t)]} \; . \tag{7}$$

In the superlattice, symmetry alone will determine whether or not this six-fold degeneracy is lifted and a different average of m^*_{et} and m^*_{el} is operative. For superlattices oriented in a <111> direction, all six minima remain equivalent by symmetry, so that no lifting of the degeneracy is expected. For superlattices oriented in either a <110> or a <100> direction, on the other hand, a four-two splitting of the six-fold degeneracy is expected. For example, in a [100]-oriented silicon superlattice the [100] and [$\bar{1}$00] minima are equivalent by symmetry as are the remaining four minima located in the (100) plane. Thus the superlattice is expected to have either two or four equivalent minima. Our calculations, discussed in Sec. III below, show, in fact, that either case can occur, with the two-minima case preferred as the thickness of the superlattice increases. In the two-minima case, one has simply

$$m^*_{eL} = m^*_{el} \tag{8}$$

and

$$m^*_{eT} = m^*_{et} \tag{9}$$

in place of an average like Eq. (7).

One can further anticipate certain general trends in the factors α_t, α_l, β_t, and β_l. When the superlattice is formed, the most pronounced effects on the band structure are the folding of the bulk bands into the mini-Brillouin zone of the superlattice and the opening of band gaps (the so-called minigaps) on the longitudinal zone-boundary faces. The latter has the clear effect of flattening the bands in the longitudinal direction and hence one expects $\alpha_l > 1$ and, for conduction band edges located along the longitudinal direction, $\beta_l > 1$. In practice, this mechanism is so effective that except for the very thin-layer cases one usually approaches the conditions

$$\alpha_l \rightarrow \infty \quad \text{and} \quad \beta_l \rightarrow \infty \, . \tag{10}$$

Consequently, the longitudinal conductivity effective masses m^*_{hL} and m^*_{eL} are always increased over the bulk, and no mobility enhancement is likely. In any transverse direction, on the other hand, such flattening of the bands does not occur and one expects to a first approximation $\alpha_t \approx 1$ and $\beta_t \approx 1$, so than definite conclusions about m^*_{ht} and m^*_{et} can't be drawn. Interestingly, however, one can easily see that even if $\beta_t = 1$,

m^*_{eT} based on Eq. (9) is significantly decreased below m^*_c from Eq. (7). Using the known bulk silicon values $m^*_l = 0.97m$ and $m^*_t = 0.19m$,[16] one finds $m^*_c = 0.26m$ and

$$\gamma_T = m^*_{eT}/m^*_c$$

$$= 0.73\ \beta_t \ . \qquad (11)$$

Thus symmetry alone could account for a 27% decrease in the transverse electron conductivity effective mass in [100]-oriented silicon superlattices. Ultimately, this effect arises because of a more favorable averaging of the relatively small transverse band mass m^*_t in the superlattice than in the bulk. Moreover, it is an effect clearly associated with the indirect nature of the bulk band gap and is absent in superlattices derived from direct-gap materials such as GaAs.

Of course, additional considerations enter the picture beyond band-edge effective masses. For example, the bulk conduction-band edges which split away and above in energy in the superlattice will always be accessible at a high enough temperature. In practice, a thermal average over a number of bands is necessary to establish the effective carrier mobility. Moreover, a different thermal average, which weights the low energy states more heavily in the superlattice than in the bulk, is usually appropriate. In the bulk, the conduction-band-edge constant-energy surfaces are ellipsoidal in shape and the density of states for a single band has the familiar form

$$N_c(E) = \frac{1}{\hbar^3\pi^2}\, m^*_t(2m^*_l)^{1/2}(E-E_c)^{1/2} \ , \qquad (12)$$

where E_c is the conduction-band edge. In the superlattice, on the other hand, the band flattening mentioned above makes the constant-energy surfaces more nearly cylindrical in shape, so that the corresponding density of states is proportional to that of a two-dimensional electron gas. For a single conduction-band edge at $\underline{k} = 0$:

$$N_c(E) = \frac{1}{\hbar^2\pi s}\, \beta_t m^*_t \ , \qquad (13)$$

which is independent of energy. Our preliminary calculations of impurity-scattering-limited electron mobility in silicon superlattices based on these considerations will be discussed in Sec. IV below.

C. Band-structure model

In formulating a band-strucutre model for silicon superlattices, we have been guided by a desire to examine general trends in this new class of systems rather than to obtain highly accurate details in any specific structures. Towards this end, we have adopted an empirical tight-binding (TB) approach which both gives a reliable bulk band structure of pure silicon and provides enough flexibility to treat all superlattice structures of interest with the variation of only a few parameters. The specific superlattice geometry considered here is illustrated in Fig. 2. We assume that the underlying tetrahedral coordination of pure bulk silicon is preserved in the superlattice, so that the position and bond length d of the nearest neighbors is unchanged. The shaded areas in Fig. 2 represent regions where either the silicon atoms have been substitutionally replaced by a second species (i.e., germanium in $Si_{1-x}Ge_x$) or the electron potential has been rigidly raised or lowered as envisaged in MOS or *nipi* superlattice structures. In the former case, we further ignor any disorder in the alloy by making a virtual crystal approximation and also any slight increase in the bond length due to the presence of the second species. Then in all cases the periodicity of the superlattice is unchanged in the transverse plane (the yz plane in Fig. 2), but in the longitiudinal direction the layers repeat with a period

$$s = n_s a/2 \ , \tag{14}$$

where a is the bulk silicon lattice constant and $2n_s$ is the number of atomic layers in each primitive cell of the superlattice. For convenience, we assume n_s to be an even integer ≥ 2. Then both the superlattice and its minizone in reciprocal space have simple tetragonal symmetry, as shown in Fig. 2. In the TB method, a small number of atomic-like basis functions is assigned to each atom and the electronic states of the solid are obtained as linear combinations of these orbitals. Following Harrison,[17] and the earlier work of Chadi and Cohen[18] on bulk silicon, we have adopted a minimal basis set of one s-like and three *p*-like orthonormal atomic orbitals. A careful study of the electronic structure of pure silicon revealed that in this basis one must retain both nearest-neighbor and second-neighbor interatomic interactions to obtain a satisfactory description of the energy bands in the vicinity of the fundamental energy-band gap. The near-neighbor

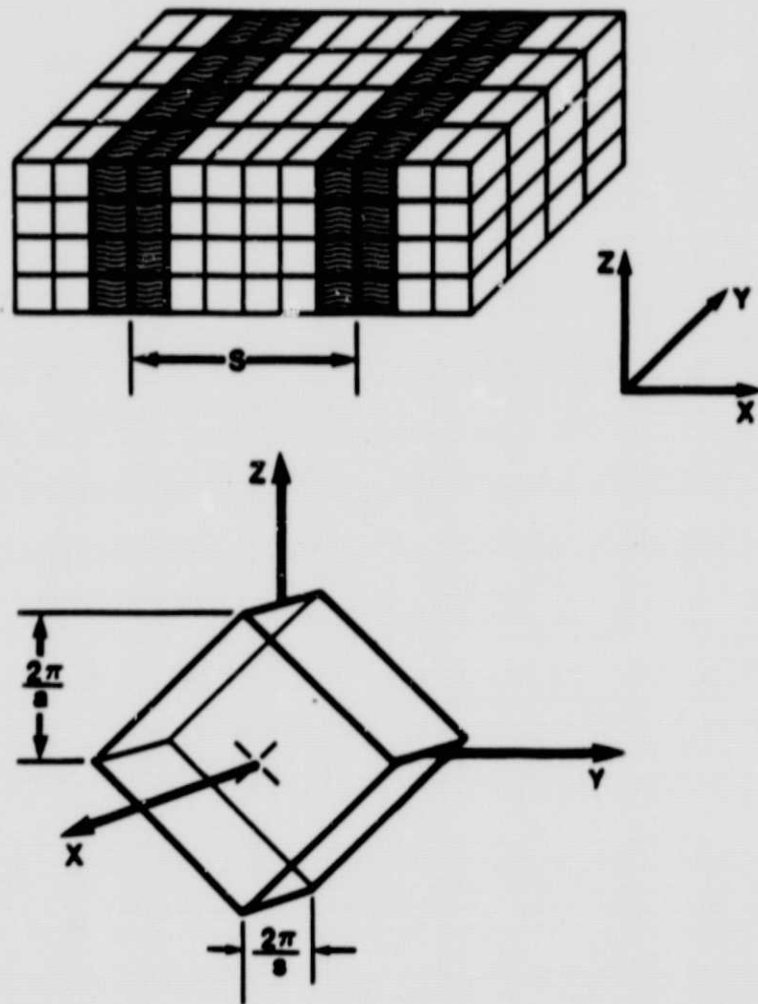

Fig. 2. Schematic drawing of the silicon superlattice geometry treated in this work. At the top is the real-space structure with period s; below is the corresponding mini-Brillouin zone (minizone) in reciprocal space.

interatomic matrix elements in covalent solids are primarily functions of bond length d in the solid and, according to Harrison,[17] may be expressed in the form

$$V_{ll'm} = \eta_{ll'm}\hbar^2/(md^2) \quad , \tag{15}$$

where $l, l' = s$ or p and the subscript m is either σ or π. We have fixed the dimensionless parameters $\eta_{ll'm}$ together with the intra-atomic energies ε_s and ε_p by fitting our bulk TB energy bands to the accurate pseudopotential results of Chelikowsky and Cohen[19] for energies up to 1 eV above the conduction-band edge. The best set of values we have thereby obtained are listed in Table I of Ref. 3.

Since we assume the bond length d of the superlattice to be identical to that of bulk silicon, the $V_{ll'm}$ are also unchanged in the superlattice. The silicon intra-atomic energies ε_s and ε_p, on the other hand, become

$$\varepsilon_s + V_s^{(s)} \tag{16}$$

and

$$\varepsilon_p + V_s^{(p)} \tag{17}$$

for the second layer of the superlattice. Fitting of the bulk silicon energy bands fixes ε_s and ε_p, so that the entire effect of the superlattice potential is incorporated into the constants $V_s^{(s)}$ and $V_s^{(p)}$. In general, these quantities represent different potentials seen by s and p electrons in the second layer. The special case

$$V_s = V_s^{(s)} = V_s^{(p)} \tag{18}$$

corresponds to the situation envisaged in an MOS or *nipi* superlattice, where the electron potential in alternating layers is raised or lowered by a constant value V_s. We have designated this as type-I behavior.[3] Another interesting case occurs for

$$V_s = - V_s^{(s)} = V_s^{(p)} \quad , \tag{19}$$

in which case *s* and *p* electrons effectively see equal and opposite superlattice potentials. Detailed consideration of the electronic structure of bulk germanium and the measured band-edge discontinuities of the Si-Ge heterostructure[20,21] suggests that this limit, which we have designated as type-II behavior,[3] is appropriate to the $Si-Si_{1-x}Ge_x$ superlattice. Our studies have further shown that in the absence of band bending at the heterojunction interface that an approximate relationship between the superlattice potential V_s and the germanium concentration is

$$V_s \approx (0.5 \pm 0.1)x \quad \text{(in eV)}. \tag{20}$$

Band bending and other nonideal interface effects may be incorporated into our model by allowing, for example, V_s to grow linearly across several layers at the interface instead of changing abruptly from zero. We have considered a number of such graded-layer calculations, but they produce results so qualitatively and quantitatively similar to the ideal case that we shall not consider this complication further in the present discussion.

III. ELECTRONIC-STRUCTURE CALCULATIONS

In the above energy-band model, the superlattice electronic structure is reduced to a function of two chemical parameters, $V_s^{(s)}$ and $V_s^{(p)}$, and three geometrical quantities: superlattice orientation, period s, and relative thickness of the two alternating layers. We have focused our attention on the limiting cases of highest applied interest: a [100]-oriented superlattice of either the type-I or type-II variety with equal layer thicknesses. The latter condition is maintained to maximize the effective superlattice strength for fixed values of V_s and n_s. Unequal layer thicknesses produce qualitatively similar but quantitatively smaller effects in all cases. Also note that for equal layer thicknesses l,

$$s = 2l \quad , \tag{21}$$

and the parameter n_s is just the number of {100} atomic planes contained in a given layer.

A. Thin-layer superlattices ($l \leq 11$ A)

In a straight-forward application of the TB method, the energy bands $E(\underset{\sim}{k})$ are obtained by direct diagonalization of the appropriate Hamiltonain matrix. In either the bulk or the superlattice, the Hamiltonian matrix is constructed from a basis of Bloch wavefunctions of the type

$$\phi_{\underset{\sim}{k}\alpha}(\underset{\sim}{r}) = \frac{1}{\sqrt{N}} \sum_i \alpha(\underset{\sim}{r}-\underset{\sim}{R}_i) e^{i\underset{\sim}{k}\cdot\underset{\sim}{R}_i} \quad , \tag{22}$$

where α is an orthonormal s, p_x, p_y, or p_z atomic orbital and the sum is over the N equivalent sites $\underset{\sim}{R}_i$ on which this orbital is centered in the crystal. If there are $2n_s$ atoms in the primative cell, then there are $8n_s$ such basis states and an $8n_s$ x $8n_s$ Hamiltonian matrix results. The detailed form of this matrix is given and discussed in the Appendix of Ref. 3.

We have performed TB electronic structure calculations for the superlattice band energies $E(\underset{\sim}{k})$ with $\underset{\sim}{k}$ in both a longitudinal [100] and a transverse [001] direction in type-I as well as type-II cases over the parameter ranges

$$0 \leq V_s \leq V_s^{max} \tag{23}$$

and

$$2 \leq n_s \leq 8 \ , \tag{24}$$

where V_s^{max} is the value of V_s for which the fundamental band gap closes. For $n_s > 8$, matrices larger than 64 x 64 would result and alternate means of calculation using complex band structures are needed, as discussed in Sec. IIIB below. The limit $n_s = 8$ corresponds to layer thicknesses of $l = 11$ A or a superlattice period of s = 22 A.

Typical results that we have obtained for the band structure in the vicinity of the fundamental energy band gap are illustrated in Fig. 3. The top panel shows the pure bulk silicon bands with the characteristic indirect gap and conduction-band edges along the <100> directions out toward the zone boundaries. The superlattice band structure may be thought of as evolving from these bulk bands in two steps. The first step is the $\underline{k}$-space translation or folding back of the bulk band structure into the minizone of the superlattice for infinitesimal V_s. The second is the additional dispersion introduced into the folded bands for finite V_s. The center panel of Fig. 3 shows the bulk silicon bands folded into the $n_s = 4$ superlattice minizone. Four of the conduction-band minima remain fixed, but the remaining two along the [100] and [$\bar{1}$00] directions are displaced to positions near $\underline{k} = 0$. When the superlattice potential V_s is increased from zero, the bands split apart, the fundamental gap narrows, and the [100] and [$\bar{1}$00] minima are further displaced in position and also lowered in energy relative to the four transverse minima, as shown in the bottom panel of Fig. 3.

The valence-band edge in the superlattice remains stationary at $\underline{k}_v = 0$, the minizone center, except for very large values of V_s (e.g., $V_s > 2.0$ eV for $n_s = 2$). The conduction-band edge $\underline{k}_c$, on the other hand, varies with both n_s and V_s, with either the characteristic two-longitudinal-minima or four-transverse-minima behavior occuring in each case. The qualitative position of $\underline{k}_c$ as a function of n_s and V_s for both type-I and type-II superlattices is illusirated in Fig. 4. Note that the two-minima case is favored as n_s increases and that in certain cases the two minima coalesce at [illegible] = 0 and a direct band gap results. The general trend suggests that [illegible] sufficiently large n_s, the band gap will become direct for all values of V_s. Our thick-layer calculations confirm this, as discussed below.

The magnitude of the fundamental band gap E_g decreases continuously as V_s is increased in all cases. The gap decreases more rapidly with V_s the larger n_s is and also somewhat faster in the type-II case than in the type-I case, as shown in Fig. 5 for $n_s = 2$ and $n_s = 8$. The latter behavior is expected on the basis of Eqs. (16)-(19), since the *s* and *p* energies are pushed together in the second layer for the type-II superlattice.

At the valence- and conduction-band edges we have also determined the longitudinal and transverse curvatures of the energy bands to obtain the effective masses m^*_{hl}, m^*_{ht}, m^*_{el}, and m^*_{et}. Relative band masses α_l, α_t, β_l, and β_t were then obtained by normalizing the calculated band masses by the calculated values of m^*_{hh}, m^*_l, and m^*_t for bulk silicon via Eqs. (1),(2),(5), and (6). The relative masses so obtained show a number of interesting and prominent features, as illustrated in Figs. 6-8. The valence-band masses α_l and α_t are smooth functions of V_s for fixed n_s since the band edge $\underset{\sim}{k}_v$ is stationary. As expected, we find $\alpha_l > 1$ for $V_s > 0$, with $\alpha_l \gg 1$ possible for large n_s. The transverse mass α_t, on the other hand, drops off very sharply with V_s from unity to about 0.8 in all cases, as shown in Figs. 6 and 7. For larger values of V_s, α_t remains less than one and is found snaller in the type-II case than in the type-I case for fixed n_s and is larger the larger n_s is for both cases. Unlike α_l and α_t, the conduction-band masses β_l and β_t are not smooth functions of V_s becasue $\underset{\sim}{k}_c$ also varies with V_s. The expected behavior $\beta_l > 1$ and $\beta_t \approx 1$ is, however, still found. Figure 8 displays β_t versus V_s for $n_s = 2$ and $n_s = 8$ in the type-II superlattice.

Whenever the conduction-band edges lie along the longitudinal x axis and Eq. (11) applies for the relative transvese electron conductivity effective mass γ_T, we indeed find $\gamma_T < 1$, so that enhanced mobility is possible. This situation occurs in our calculations for $n_s \geq 6$ in the type-I superlattice and $n_s \geq 4$ in the type-II superlattice. Figure 9 shows the variation of γ_T, $\gamma_T^{-1/2}$, and $\gamma_T^{-5/2}$ with V_s for $n_s = 8$ in the type-II superlattice. The quantities $\gamma_T^{-1/2}$ and $\gamma_T^{-5/2}$ are the ideal enhancement factors expected for impurity-scattering-limited electron mobility and phonon-scattering-limited electron mobility, respectively, if all other things are equal.

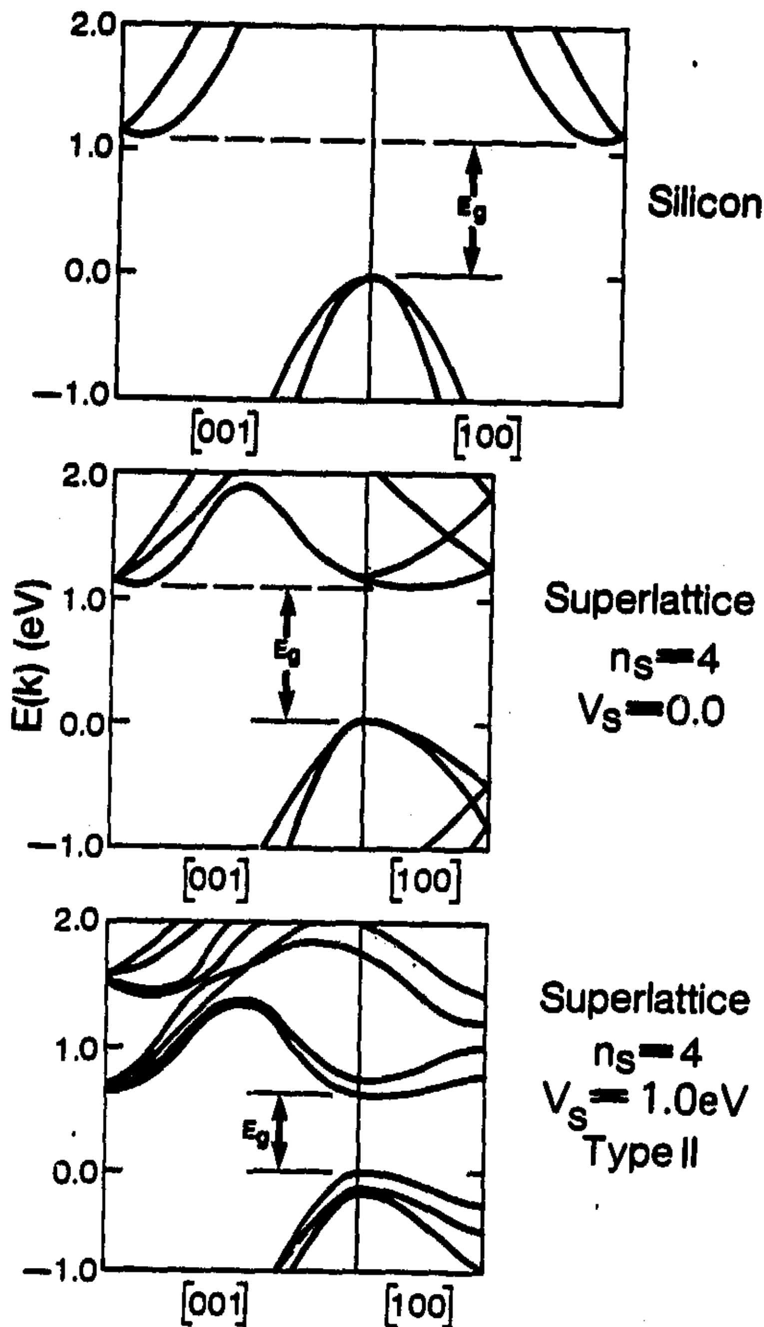

Fig. 3. Evolution of the superlattice electronic structure in the longitudinal [100] and transverse [001] directions from the bulk energy bands for a typical case. Top panel, the bulk silicon bands; center panel, folded bulk bands in the $n_s = 4$ superlattice minizone; bottom panel, type-II superlattice bands for a finite superlattice potential V_s.

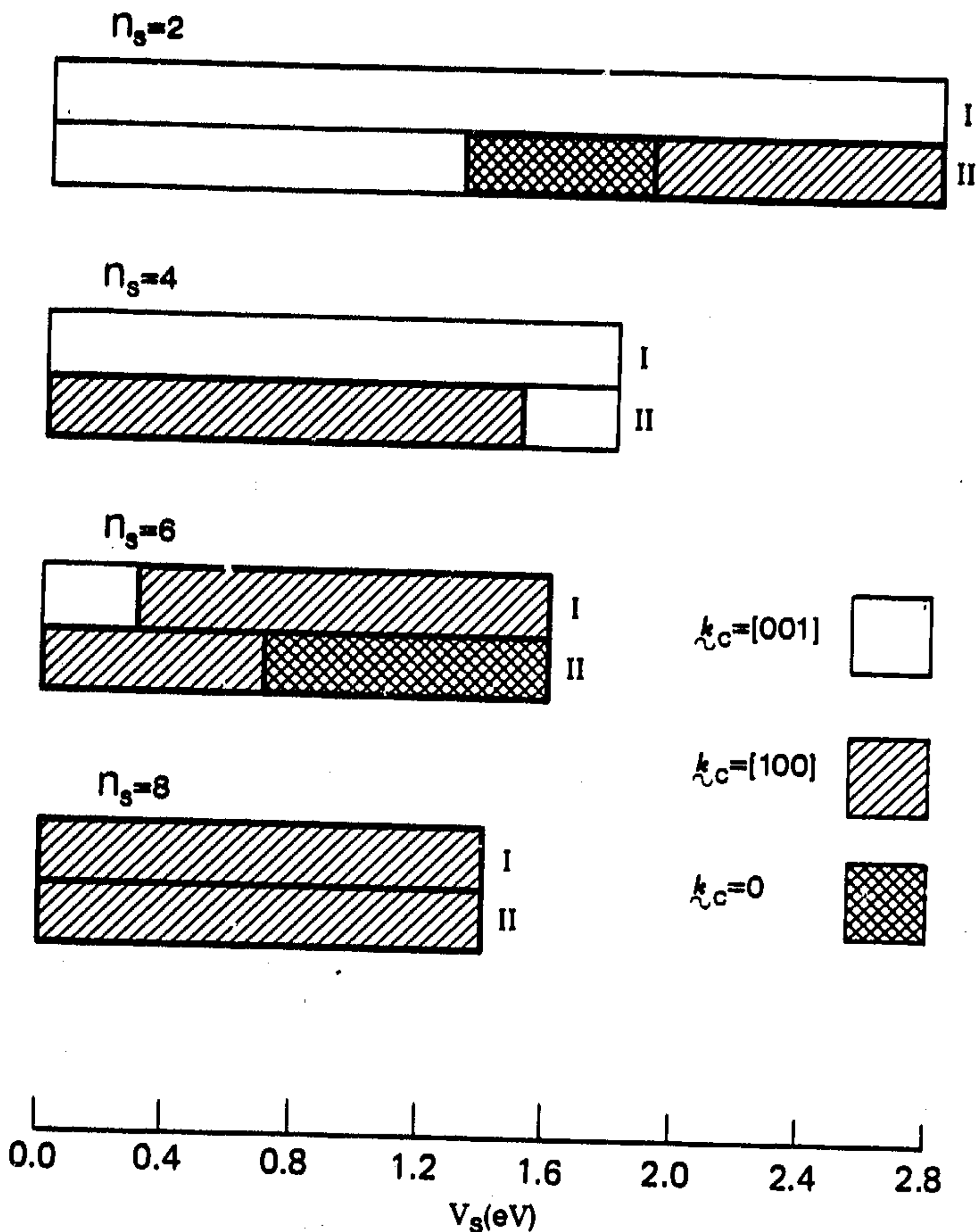

Fig. 4. Qualitative position of the conduction-band edge in both type-I and type-II silicon superlattices as a function of n_s and V_s. The position $\underset{\sim}{k}_c$ = [001] actually corresponds to four equivalent edges symmetrically centered along the the transverse y and z axes; $\underset{\sim}{k}_c$ = [100] corresponds to two equivalent edges symmetrically centered along the x axis near $\underset{\sim}{k}$ = 0; $\underset{\sim}{k}_c$ = 0 corresponds to the special case where the latter two edges coalesce into a single point at the center of the minizone.

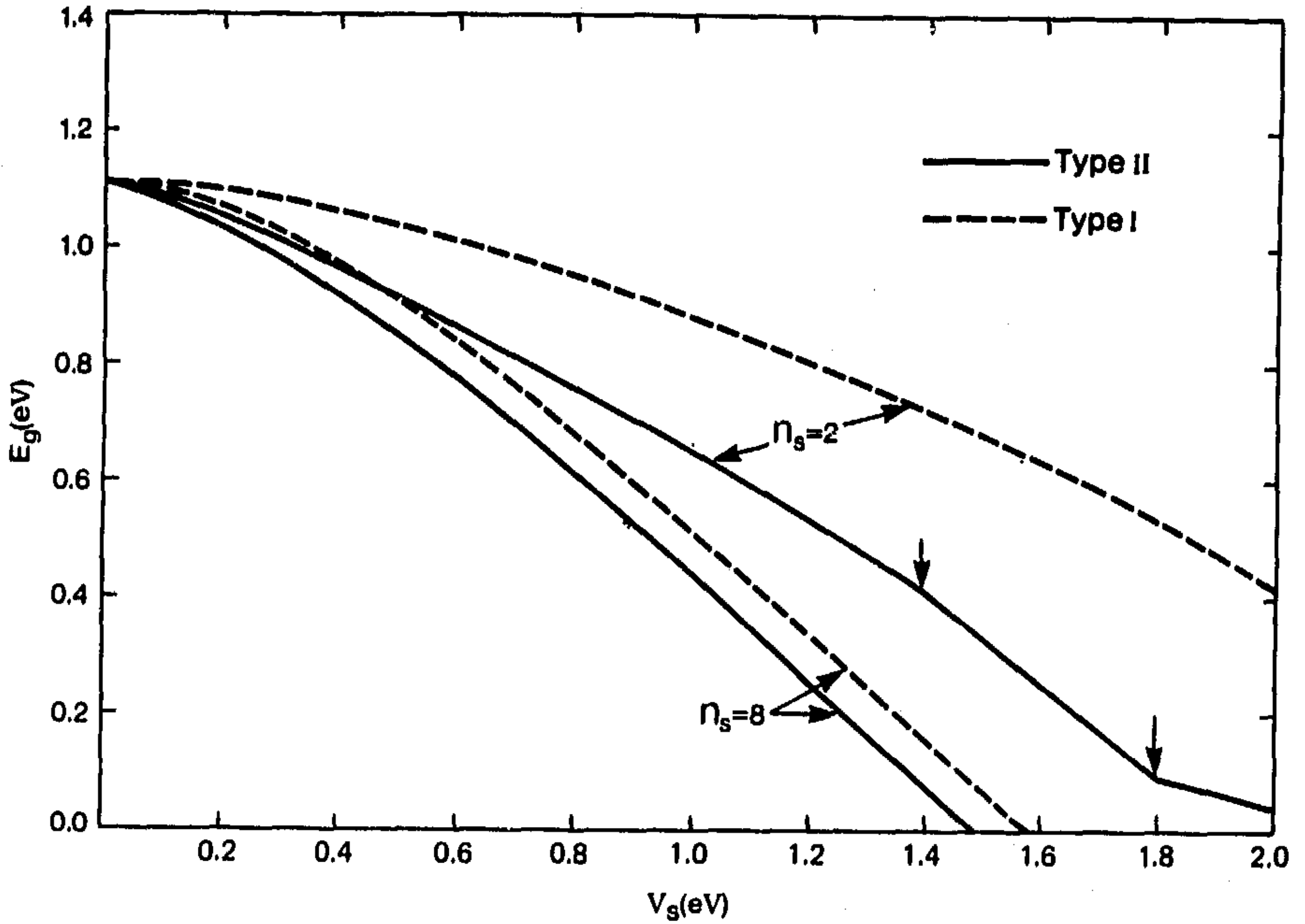

Fig. 5. Variation of the fundamental energy band gap E_g with V_s for $n_s = 2$ and $n_s = 8$ in type-I and type-II superlattices. The vertical arrows indicate places where the conduction-band edge position $\underline{k}_c$ changes discontinuously (see Fig. 4).

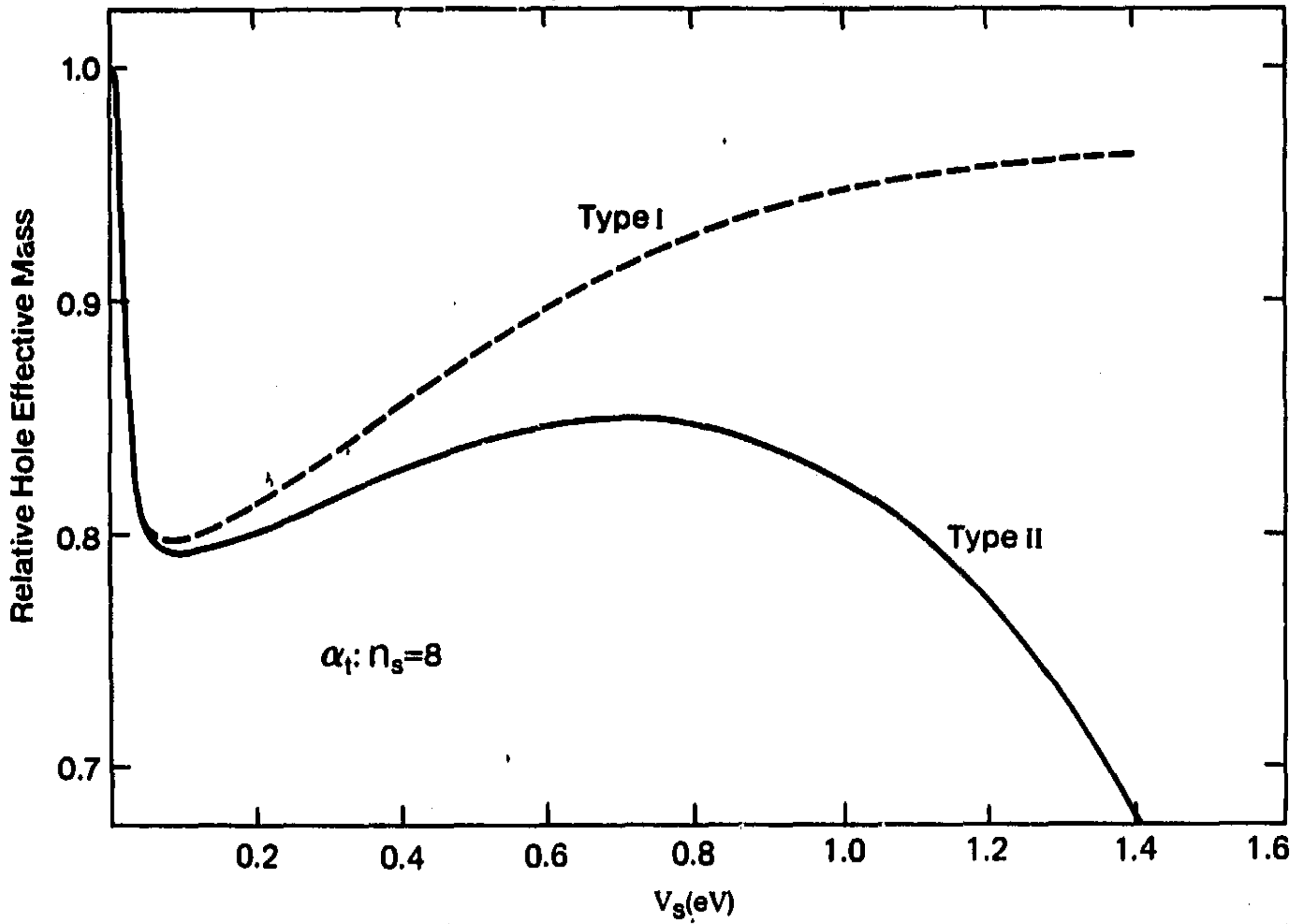

Fig. 6. Relative transverse hole band mass α_t vs V_s for n_s = 8 in type-I and type-II superlattices.

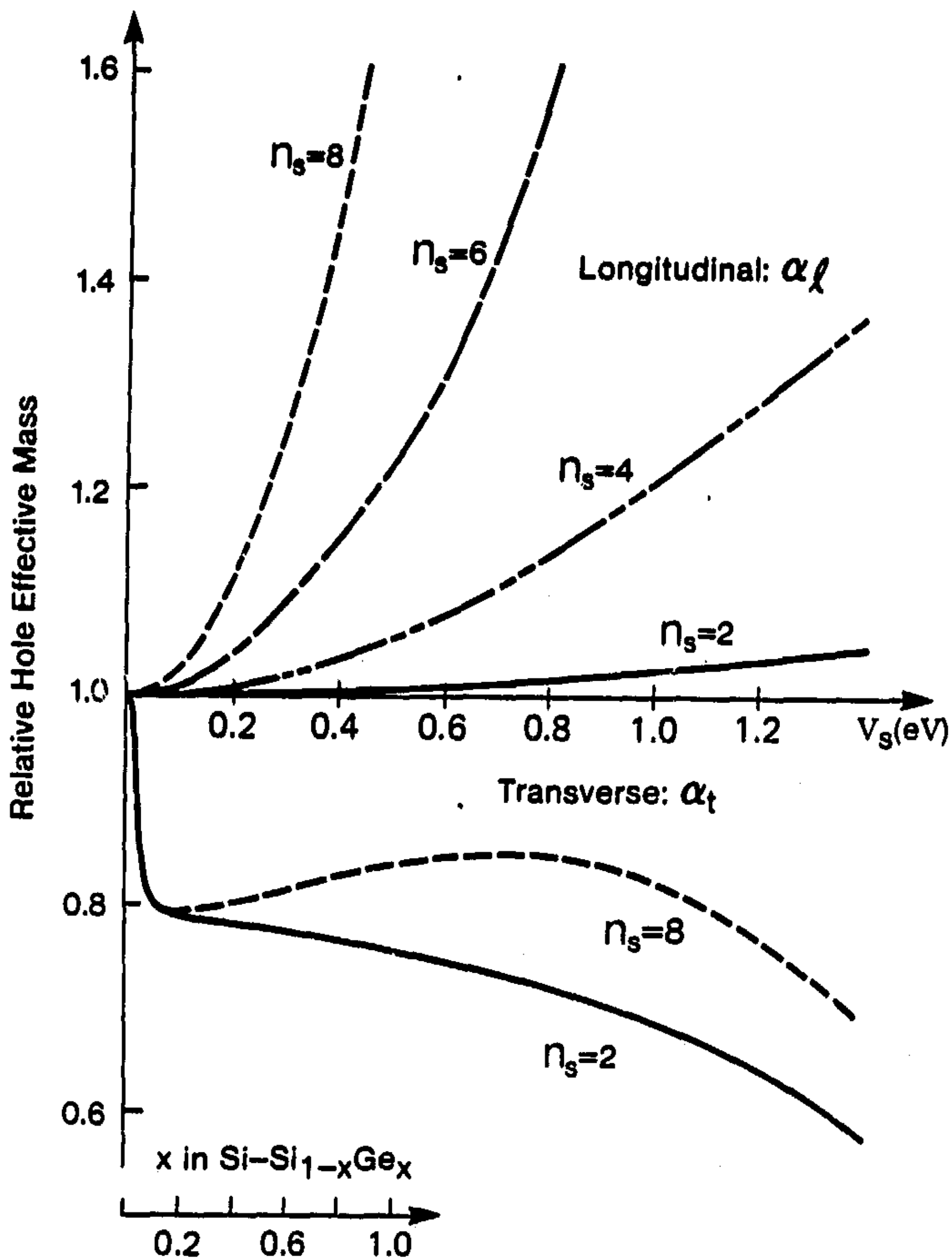

Fig. 7. Relative longitudinal α_l and transverse α_t hole band masses as a function of n_s and V_s in the type-II superlattice. The scale at the bottom of the figure relates the concentration x to V_s via Eq. (20).

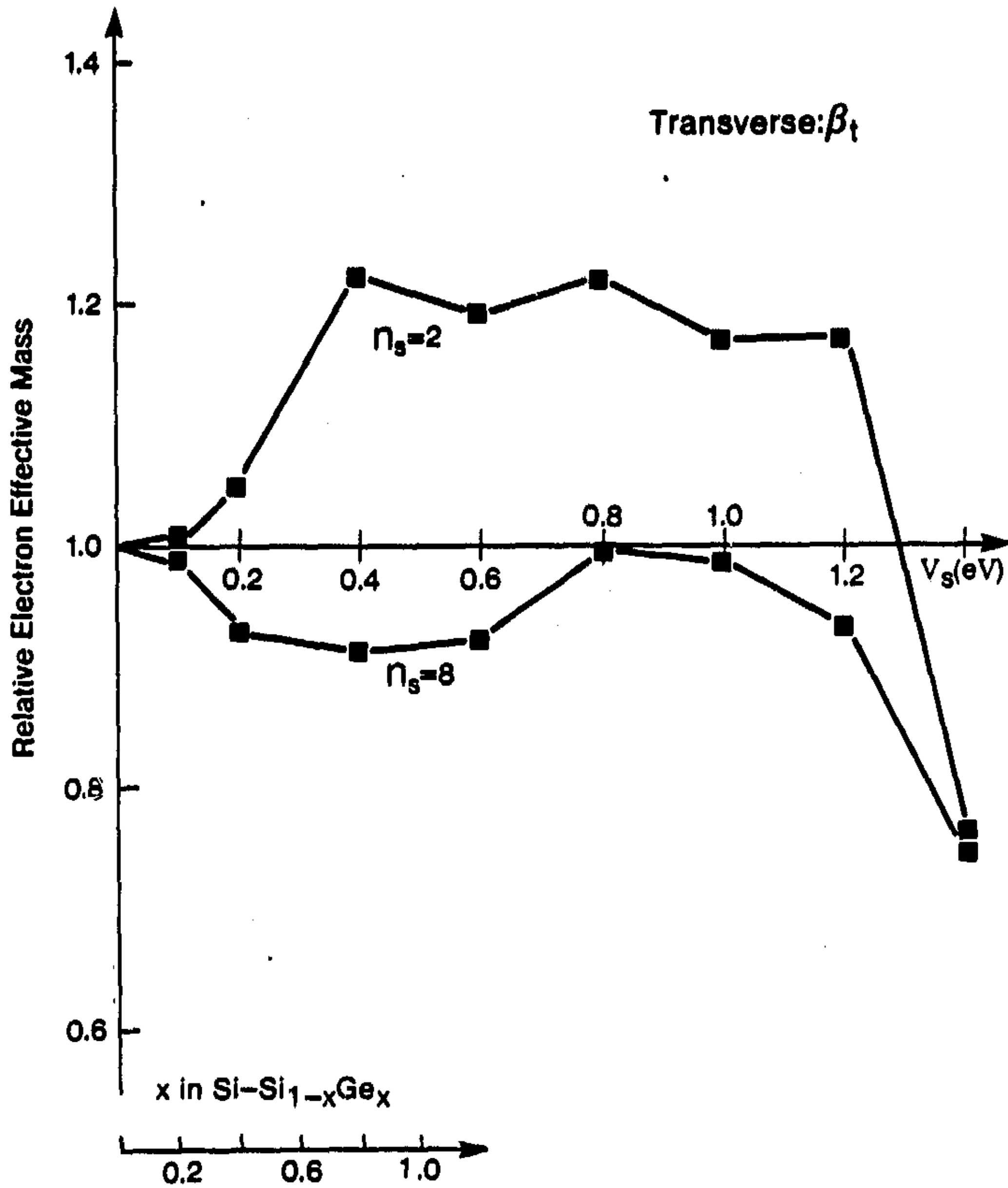

Fig. 8. Relative transverse electron band mass β_t vs V_s for n_s = 2 and n_s = 8 in the type-II superlattice. The lower scale is as in Fig. 7.

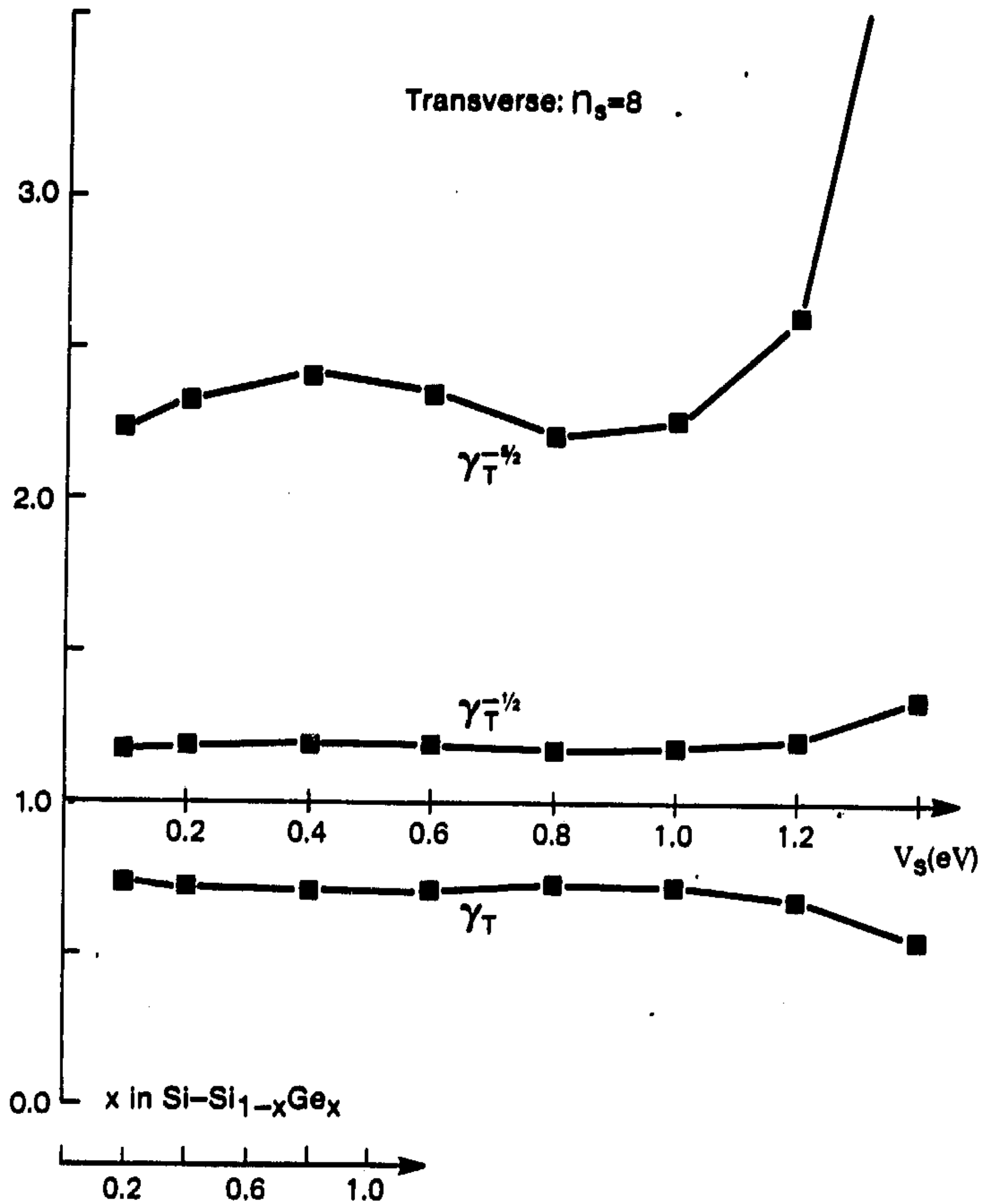

Fig. 9. Relative transverse electron conductivity effective mass γ_T and impurity-scattering-limited and phonon-scattering-limited enhancement factors $\gamma_T^{-1/2}$ and $\gamma_T^{-5/2}$ vs V_s for n_s = 8 in the type-II superlattice. The lower scale is as in Fig. 7.

B. Thicker-layer superlattices ($11 \le l \le 110$ A)

Because the TB Hamiltonian matrix increases in size proportional to layer thickness, the calculation of the superlattice electronic structure in this manner becomes intractable for even modestly thick layers. The complex band-structure technique of Schulman and Chang[22] nicely overcomes this difficulty. In this method, one views the superlattice as being composed of bulk regions in each layer separated by interface planes, as shown in Fig. 10. The number of atomic interface planes is taken such that the atoms in bulk regions I and II are not directly coupled: for second-neighbor interactions, two planes at each interface are required. One then capitalizes on the fact that the solutions to Schrödinger's equation are local and hence in the bulk regions must be some linear combination of bulk states including both extended Bloch states (real $\underset{\sim}{k}$) and evanescent states (complex $\underset{\sim}{k}$). For a given energy E, there are in our case 16 possible $\underset{\sim}{k}$ states in each bulk region. These states, together with two-dimensional Bloch sums of atomic orbitals centered on the interface-plane atoms, can be used to expand the superlattice wavefunction in the form

$$\Psi_{\underset{\sim}{q}}(\underset{\sim}{r},E) = \frac{1}{\sqrt{N_L}}\sum_{\underset{\sim}{L}} e^{i\underset{\sim}{q}\cdot\underset{\sim}{L}}\Big[\sum_{\sigma,i} A^{\sigma}_{\underset{\sim}{k}_i}(\underset{\sim}{q})\psi^{\sigma}_{\underset{\sim}{k}_i}(\underset{\sim}{r}-\underset{\sim}{L},E)$$

$$+ \sum_{j,\alpha} B^{j}_{\alpha}(\underset{\sim}{q})\phi^{j}_{\underset{\sim}{k}_{\parallel}\alpha}(\underset{\sim}{r}-\underset{\sim}{L})\Big] , \qquad (25)$$

where $\underset{\sim}{q} = q_x\underset{\sim}{x} + \underset{\sim}{k}_{\parallel}$ is the superlattice wavevector, $\underset{\sim}{L} = ns\underset{\sim}{x}$, with n an integer, $\underset{\sim}{k}_i = k^i_x\underset{\sim}{x} + \underset{\sim}{k}_{\parallel}$ is a bulk wavevector ($i = 1,16$), $\psi^{\sigma}_{\underset{\sim}{k}_i}$ is the corresponding bulk wavefunction for region σ (σ = I,II in Fig. 10), and $\phi^{j}_{\underset{\sim}{k}_{\parallel}\alpha}$ is a two-dimensional Bloch state for interface plane j ($j = S_1,S_2,S_3,S_4$ in Fig. 10) and atomic orbital α ($\alpha = s,p_x,p_y,p_z$). The resulting Hamiltonian matrix is of size 48 x 48 independent of layer thickness.

The price that must be paid for a fixed Hamiltonian-matrix size is an energy dependent basis, requiring an iteration procedure to calculate the superlattice band structure self-consistently. For given values of n_s and V_s, one fixes the superlattice wavevector $\underset{\sim}{q}$ and selects a trial energy $E = E_t$ to to be used in Eq. (25). For the chosen E_t, the 16 bulk states for each region are obtained. This information is contained in the complex band structure of the bulk material,[23,24] which need only be generated once for each layer. Figure 11 shows the [100] complex band

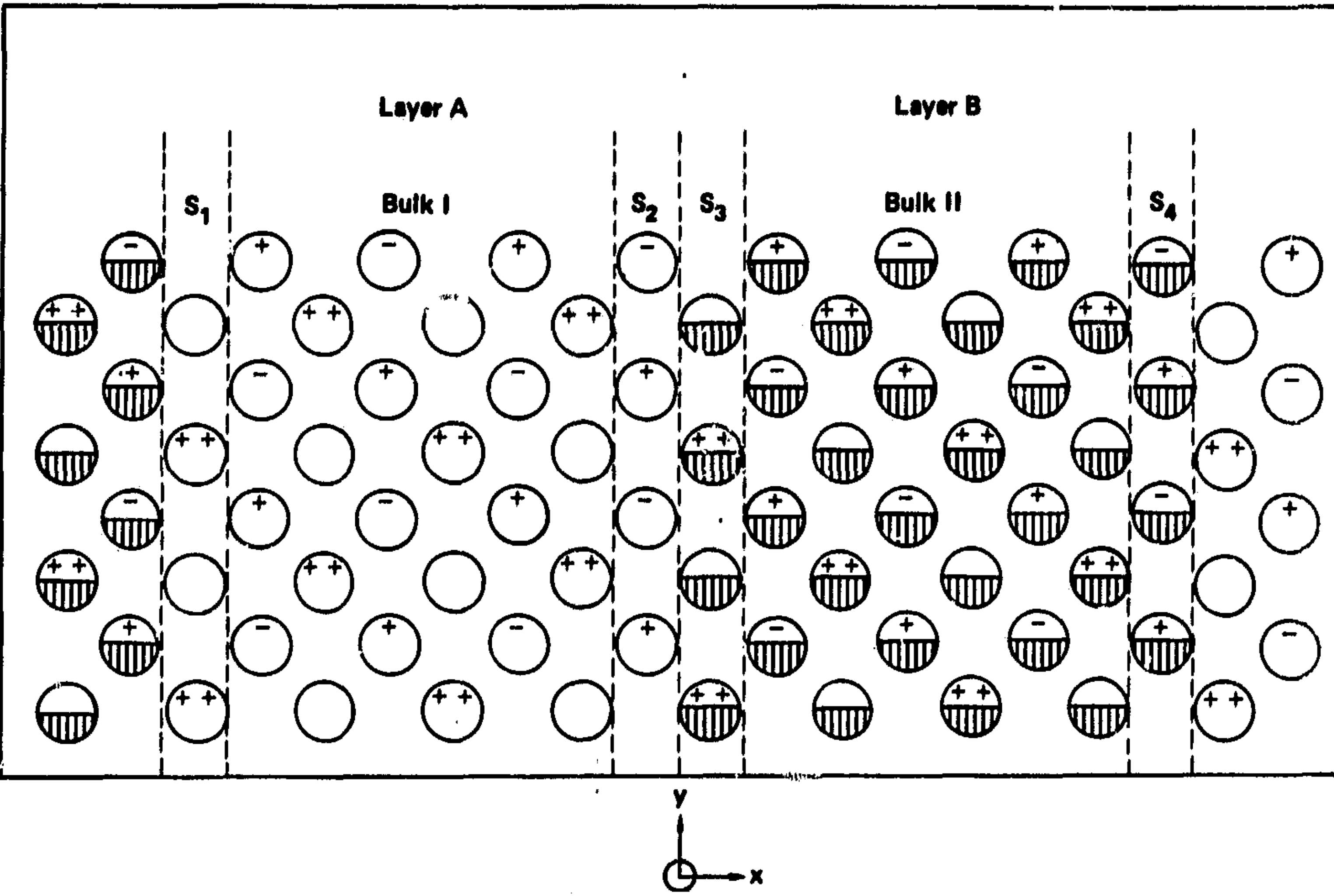

Fig. 10. Schematic diagram of the $n_s = 8$ superlattice geometry, showing the projection of four planes of atoms onto the $z = 0$ plane. The unhatched circles represent the Si atoms of layer A, while the hatched circles represent the atoms of layer B. Atoms belonging to the planes $z = -a/4$, $a/4$, and $a/2$ are marked $-$, $+$, and $++$, respectively. The bulk regions I and II and interface layers S_1, S_2, S_3, and S_4 apply to the complex band-structure technique discussed in the text.

structure of bulk silicon. The 48 x 48 superlattice Hamiltonian is then set up and diagonalized to obtain the true superlattice energy E_s for the assumed basis. One iterates this procedure until $E_s = E_t$ to some acceptable tolerance. In our procedure, an accuracy of 10^{-5} eV in energy is achieved with typically 5 iterations in less than 1 minute of cpu time. By varying q, the complete superlattice band structure may be mapped out in this way.

Our tight-binding complex band-structure method (TB-CBM) improves upon that of Schulman and Chang[22] in two important ways. First, our tight-binding model includes second-neighbor interactions as well as the first-neighbor interactions considered by them. Second, in constructing the superlattice Hamiltonian from the basis (25), we have included certain finite-layer corrections[4,5] to the bulk regions that are necessary to make the method exact and were neglected by Schulman and Chang. These corrections become vanishingly small as $n_s \to \infty$, but significantly affect fine details of the band structrure such as effective masses for the range of n_s considered here.

TB-CBM calculations of the silicon superlattice band structure have been carried out for $8 \leq n_s \leq 80$ ($11 \leq l \leq 110$ A) and $0 \leq V_s \leq 1.0$ eV for both the type-I and type-II cases. In particular, the magnitude of the fundamental band gap, conduction band-edge positions, and band-edge effective masses have been obtained over these parameter ranges. For $n_s = 8$, the results obtained are identical to those from the thin-layer TB calculations, confirming the exactness of our approach. For $n_s > 8$, the trends extablished in the thin-layer calculations are continued. The variation of the band gap magnitude E_g with V_s and n_s is shown in Figs. 12 and 13 for thick-layer type-I and type-II superlattices, respectively. As expected, E_g continues to decrease with increasing V_s and n_s, but the E_g versus V_s curve quickly saturates for large n_s. Extrapolation of the $n_s = 80$ curves in Figs. 12 and 13 suggests that the band gap will close for $V_s = 1.11$ eV, the bulk silicon band gap, in the limit $n_s \to \infty$, as required in the type-I case.

The positions of the two $n_s = 8$ conductions band edges remain along the x axis for $n_s > 8$. For $n_s \geq 32$ ($l \geq 44$ A), the two edges permanently coalesce at Γ and a stable direct band gap results. This situation is illustrated in Fig. 14, where the complete longitudinal [100] and transverse [001] band structure E(q) in the vicinity of the fundamental gap is plotted in a typical thick-layer case. The energy difference Δ between the X and Γ conduction band edges always remains small, however, (≤ 0.0065 eV = 75 K) and eventually declines back to zero as $n_s \to \infty$, as shown in Fig. 15.

For $n_s > 8$, the infinite limits of Eq. (10) have been essentially reached for the longitudinal electron and hole effective masses at any

finite V_s. The transverse effective mass factors α_t and β_t also saturate to values near unity for $n_s > 64$. The thick-layer, type-I and type-II superlattice values of α_t vs V_s are plotted in Fig. 16, while the thick-layer, type-II values of β_t vs V_s are plotted in Fig. 17. The corresponding type-I values of β_t are virtually identical to the latter. With $\beta_t \approx 1$, one has $\gamma_T \approx 0.73$ and the impurity-scattering-limited and phonon-scattering-limited enhancement factors, $\gamma_T^{-1/2}$ and $\gamma_T^{-5/2}$, saturate at values of 1.17 and 2.20, respectively, as shown in Fig. 18.

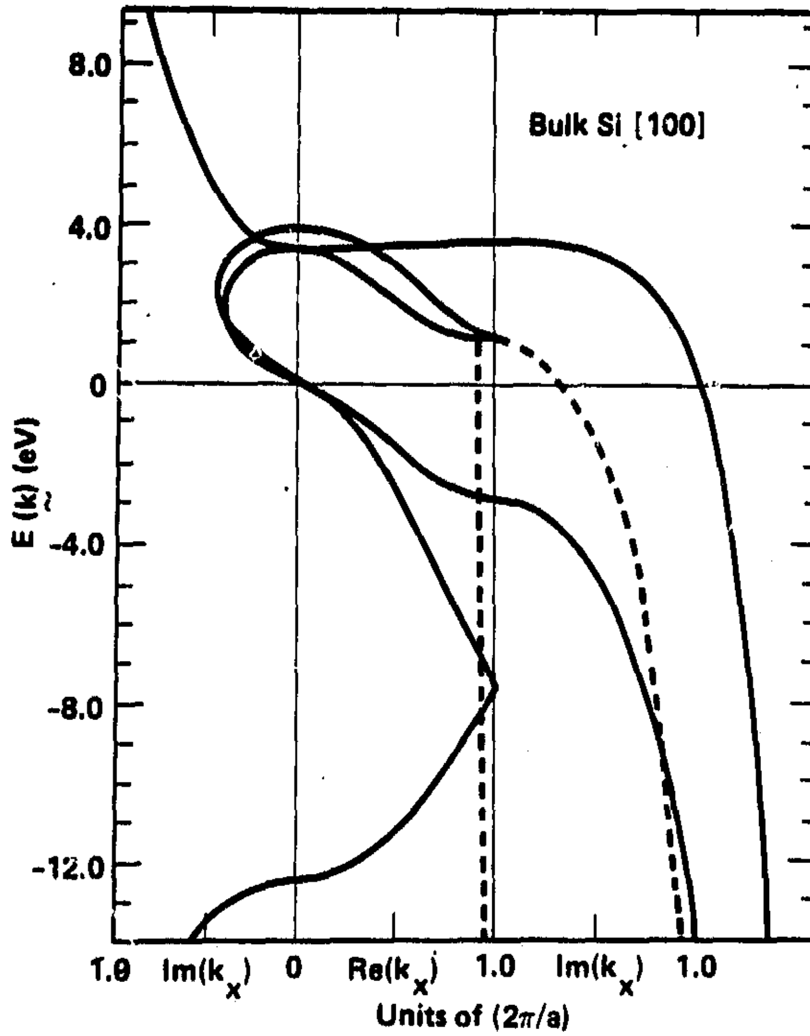

Fig. 11. Complex band structure of bulk silicon in the [100] direction with $\underset{\sim}{k} = k_x \underset{\sim}{x}$. Left panel: complex bands with $Re(k_x) = 0$; center panel: real bands, with $Im(k_x) = 0$; right panel: complex bands, with $Re(k_x) = 2\pi/a$.

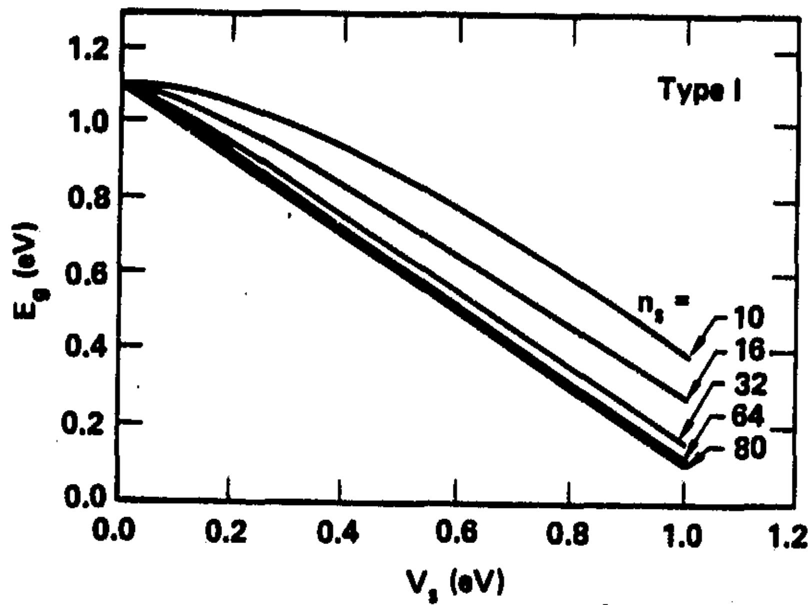

Fig. 12. Variation of the fundamental energy band gap E_g with V_s for the thick-layer type-I superlattice at five layer thicknesses. Compare with Fig. 5

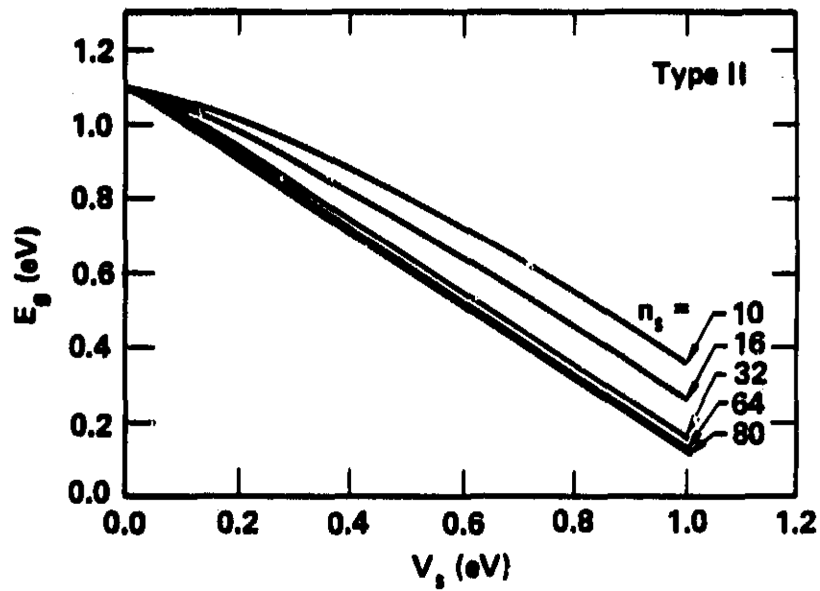

Fig. 13. Variation of the fundamental energy band gap E_g with V_s for the thick-layer type-II superlattice at five layer thicknesses. Compare with Fig. 5

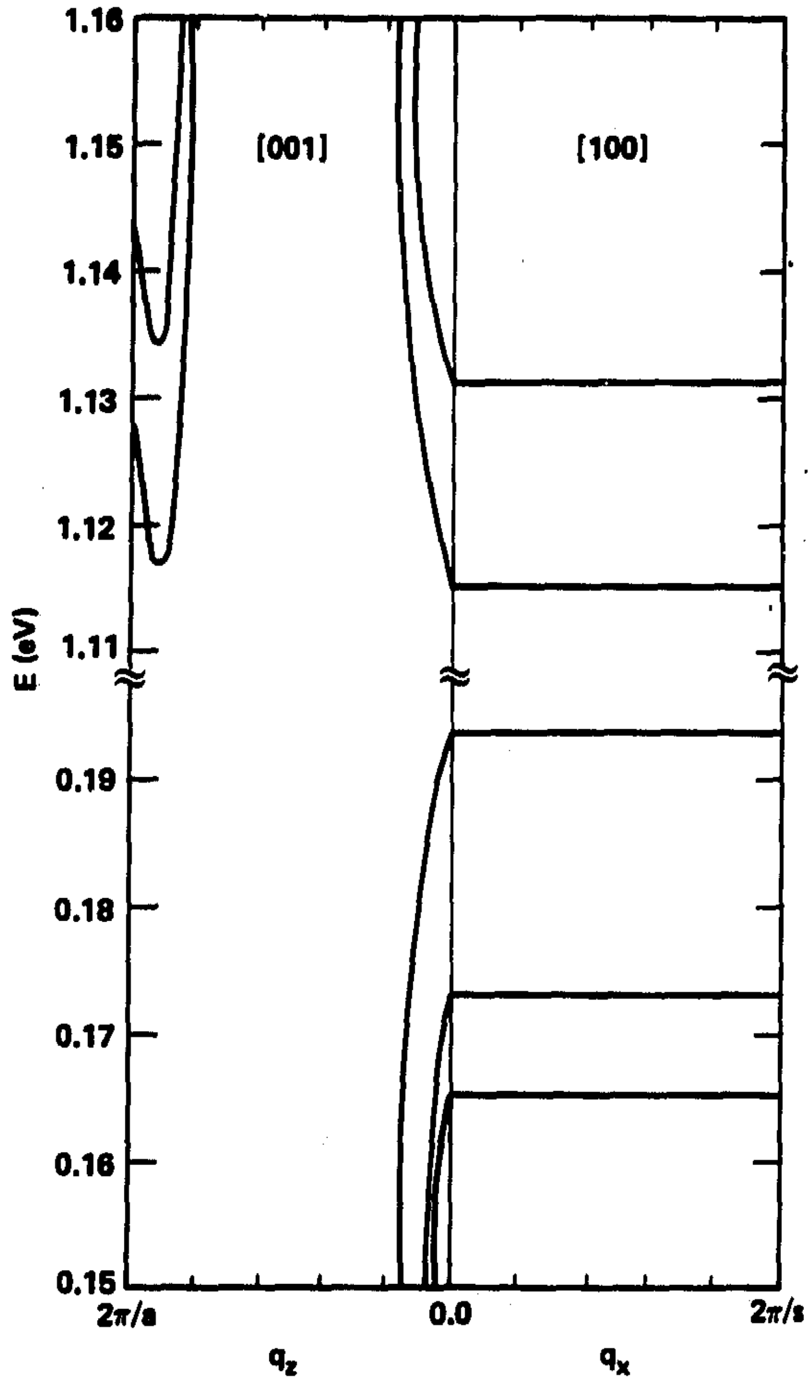

Fig. 14. Longitudinal [100] and transverse [001] band structures near the fundamental band gap of a type-II superlattice with n_s = 64 and V_s = 0.2 eV. The bands shown are those thermally accessible to mobile charge carriers at room temperature.

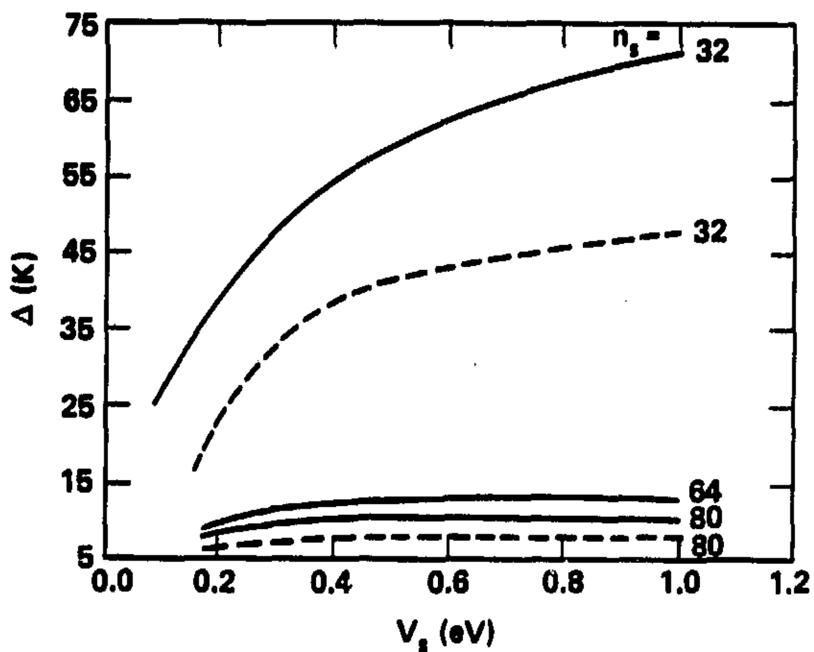

Fig. 15. Energy difference Δ between the X and Γ-point conduction-band minima vs V_s for various type-I and type-II superlattices. (Solid lines, type-I and dashed lines, type-II.) The n_s = 64, type-II result has been omitted for clarity.

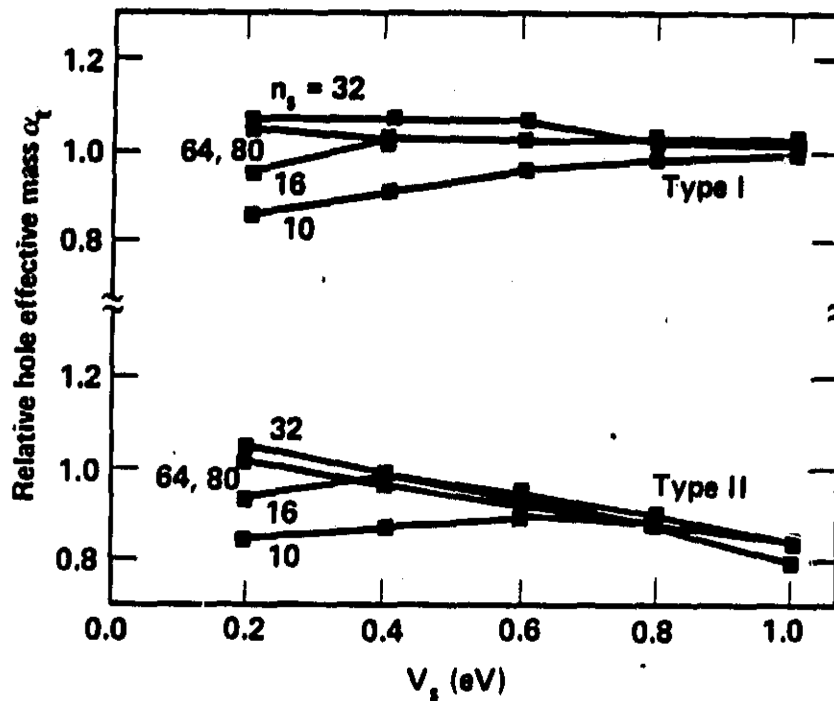

Fig. 16. Relative transverse hole effective mass α_t vs V_s for various n_s in thick-layer type-I and type-II superlattices. Compare with Figs. 6 and 7.

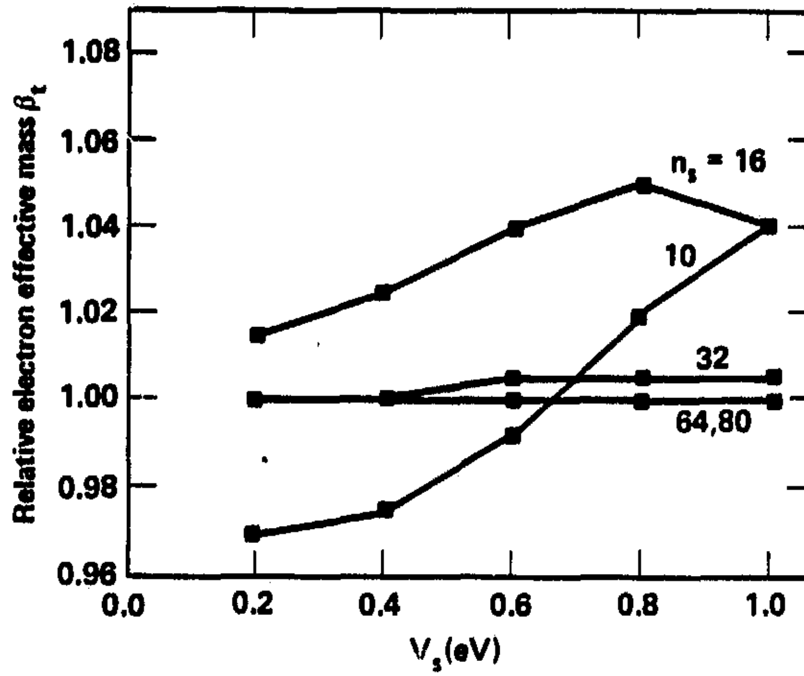

Fig. 17. Relative transverse electron effective mass β_t vs V_s for various n_s in the thick-layer, type-II superlattice. Compare with Fig. 8.

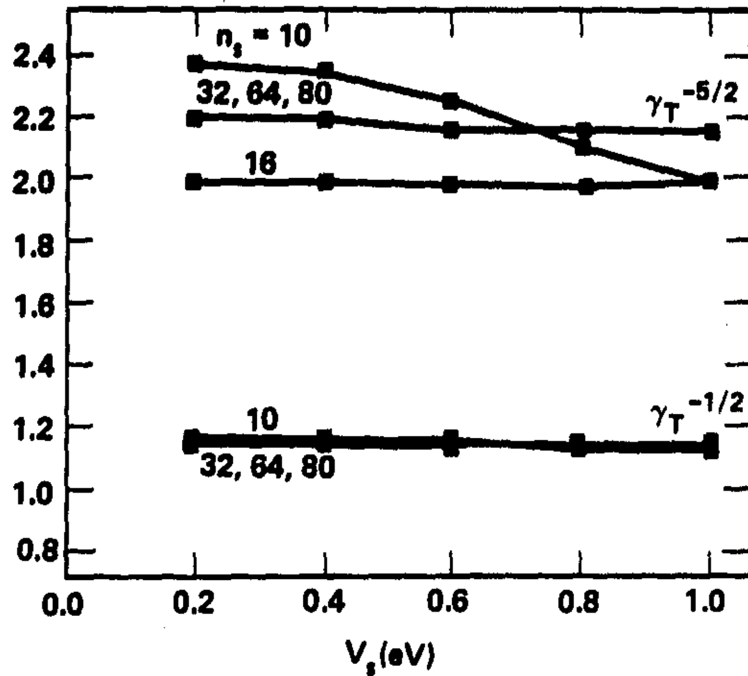

Fig. 18. Impurity-scattering-limited and phonon-scattering-limited enhancement factors $\gamma_T^{-1/2}$ and $\gamma_T^{-5/2}$ vs V_s for various n_s in the thick-layer, type-II superlattice. The n_s = 16 result for $\gamma_T^{-1/2}$ has been omitted for clarity. Compare with Fig. 9.

IV. IMPURITY-SCATTERING-LIMITED ELECTRON MOBILITY

In our present studies, we have considered ionized impurity scattering of electrons from the screened Coulomb potential

$$v_I(r) = -\frac{e^2}{\kappa}\frac{e^{-\lambda r}}{r}, \tag{26}$$

where κ is the dieletric constant of the host and λ^{-1} is the Debye length, $\lambda^2 = (4\pi n_I e^2/\kappa k_B T)$, for uniform doping to a concentration n_I. In bulk silicon, where the density of states (12) is operative for each conduction band edge, the corresponding mobility of nondegenerate electrons is well approximated by the standard form[26]

$$\mu_B = \frac{32\kappa^2}{\sqrt{8\pi^3}e^3}\frac{(k_B T)^{3/2}}{n_I (m_c^*)^{1/2}} G_B(n_I, T, m_c^*), \tag{27}$$

where G_B is a slowly varying function of n_I, T, and m_c^*. In the superlattice, a similar calculation, but with a constant density of states like (13), yields for the $i^{\underline{th}}$ conduction band

$$\mu_{SL}^i = \frac{15 s\kappa^{3/2}}{4\pi\sqrt{2}e^2}\frac{k_B T}{(n_I m_{eT}^*)^{1/2}} G_{SL}(n_I, T, m_{eT}^*), \tag{28}$$

neglecting interband scattering. Here G_{SL} is also a slowly varying function and m_{eT}^* is the appropriate transverse conductivity mass for the $i^{\underline{th}}$ band. The inverse-square-root effective-mass dependence of the bulk is recovered, as expected, but the temperature and impurity concentration dependencies now reflect the two-dimensional nature of the transport. Summing contributions from all thermally accessible conduction bands, the average electron drift mobility in the superlattice is given by

$$\mu_{SL} = \sum_i n_i \mu_{SL}^i / n_I \quad , \tag{29}$$

where n_i is the electron concentration in the ith band. For T ≤ 300 K, the conduction bands which must be included in Eq. (29) are shown in Fig. 14.

For a typical silicon superlattice, the calculated relative mobility μ_{SL}/μ_B based on Eqs. (27)-(29) is plotted in Fig. 19 as a function of n_I for various values of T and in Fig. 20 as a function of T for various values of n_I. It can be seen that at low temperatures, where impurity scattering dominates other scattering mechanisms, an enhancement in electron mobility is indeed possible for sufficiently high carrier concentrations. The qualitative variations found with n_I and T are most easily understood by considering the high temperature limits of Eqs. (27) and (28), from which one finds

$$\mu_{SL}/\mu_B = C_1 \left(\frac{n_I}{T}\right)^{1/2} \ln\left(\frac{C_2 T^2}{n_I}\right) , \tag{30}$$

where C_1 and C_2 are constants. For a fixed T in the range of interest, this function increases to a maximum for some n_I and then decreases monotonically. Similarly, for a fixed n_I, this function increases to a maximum for some T and then decreases.

The corrresponding Hall mobility in the superlattice may be calculated by replacing Eq. (29) by the average

$$\sum_i r_i n_i (\mu_{SL}^i)^2 \Big/ \sum_i n_i \mu_{SL}^i , \tag{31}$$

where r_i is a weighting factor reflecting the energy dependence and anisotropy of the scattering. Our calculated relative Hall mobility is plotted in Fig. 21 as a function of n_I for various values of T and in Fig. 22 as a function of T for various values of n_I, for the same superlattice parameters as in Fig. 19. Similar magnitudes and trends are clearly seen.

The results presented in Figs. 19-21 should be considered as upper limits to what could be expected in real systems. Neglected factors will tend to reduce the actual mobility, in particular, interband scattering at high carrier concentrations and alloy scattering in the case of a $Si\text{-}Si_{1-x}Ge_x$ superlattice. At the same time, these results take only partial advantage of the unique reduced-effective-mass

enhancement mechanism in silicon superlattices, which should be much more effective in the case of phonon scattering.

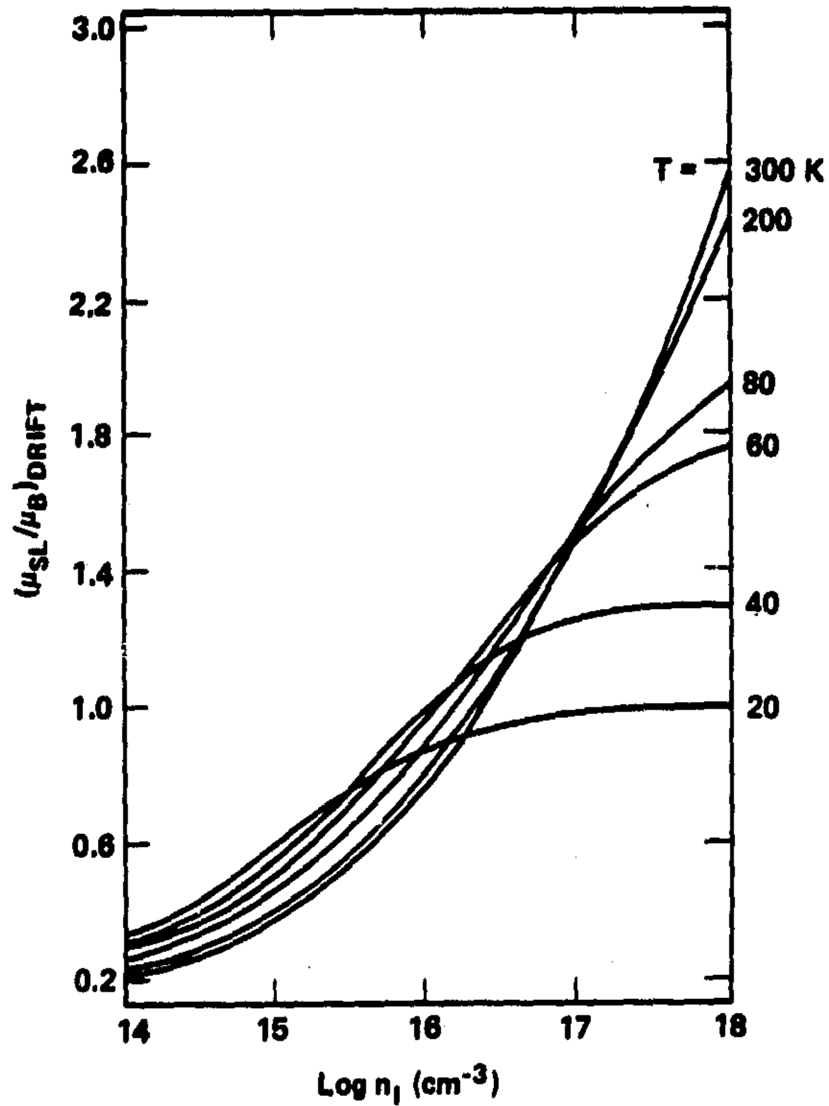

Fig. 19. Variation of the impurity-scattering-limited electron drift mobility with donor concentration n_I at various temperatures for a type-II superlattice, where n_s = 64 and V_s = 0.2 eV, relative to bulk silicon.

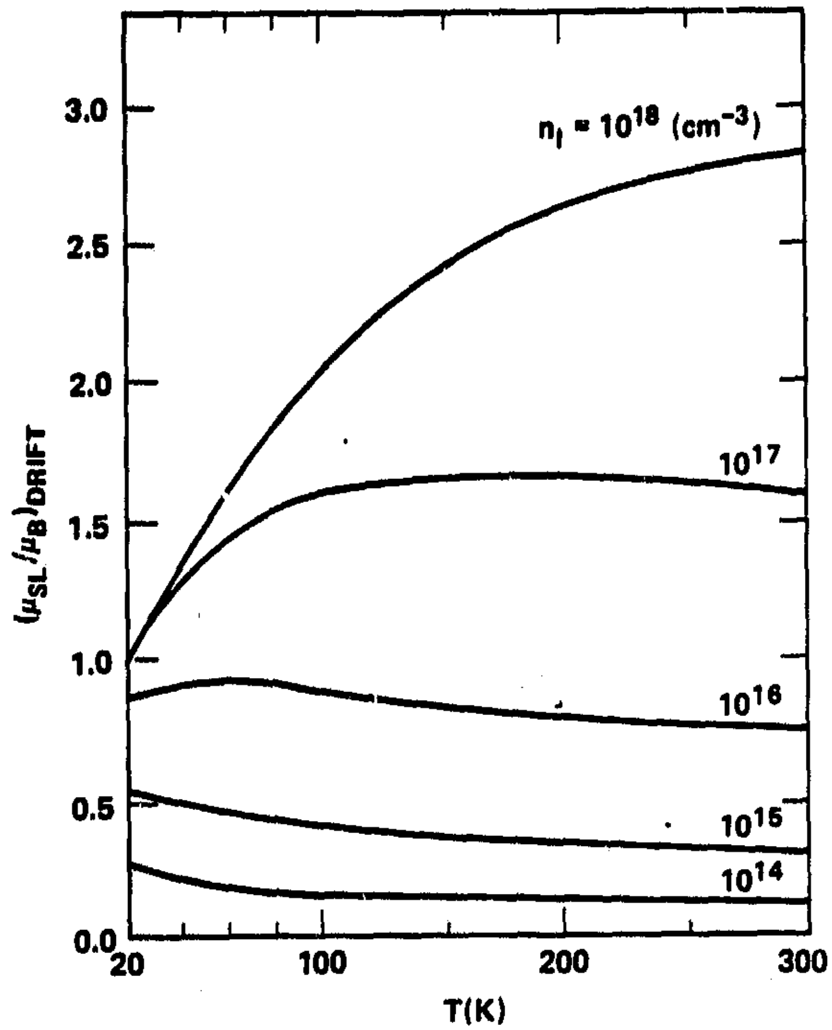

Fig. 20. Variation of the impurity-scattering-limited electron drift mobility with temperature T for various donor concentrations, as in Fig. 19.

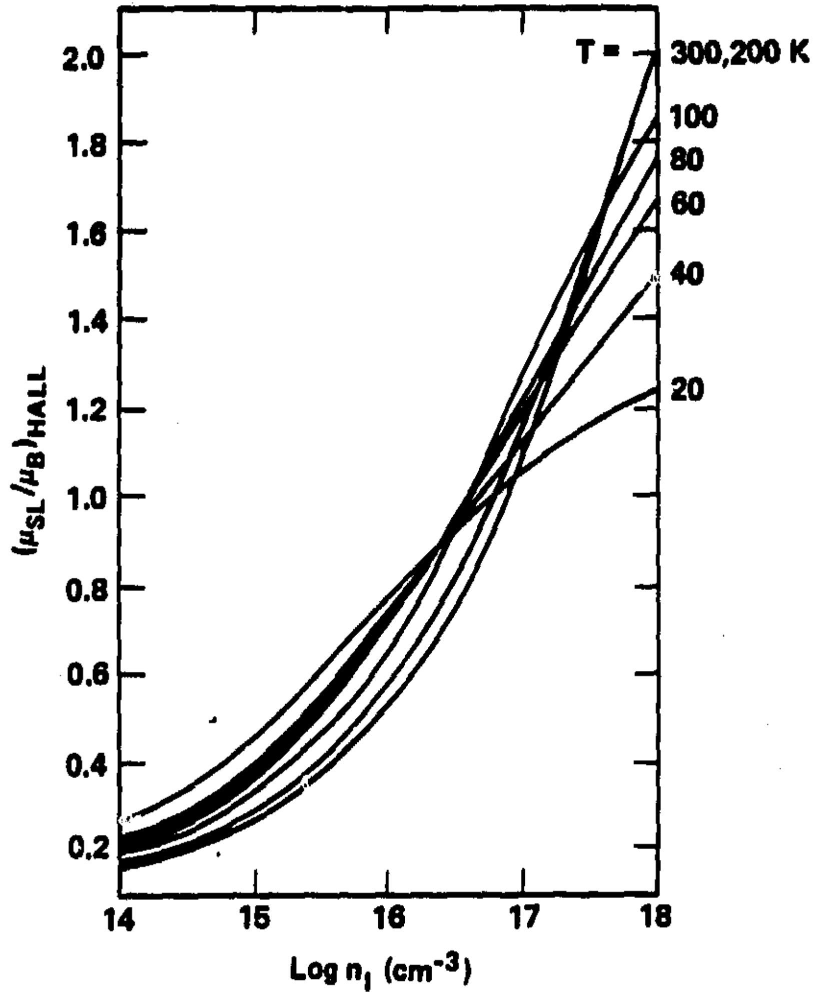

Fig. 21. Variation of the impurity-scattering-limited electron Hall mobility with donor concentration n_I at various temperatures for a type-II superlattice, where n_s = 64 and V_s = 0.2 eV, relative to bulk silicon.

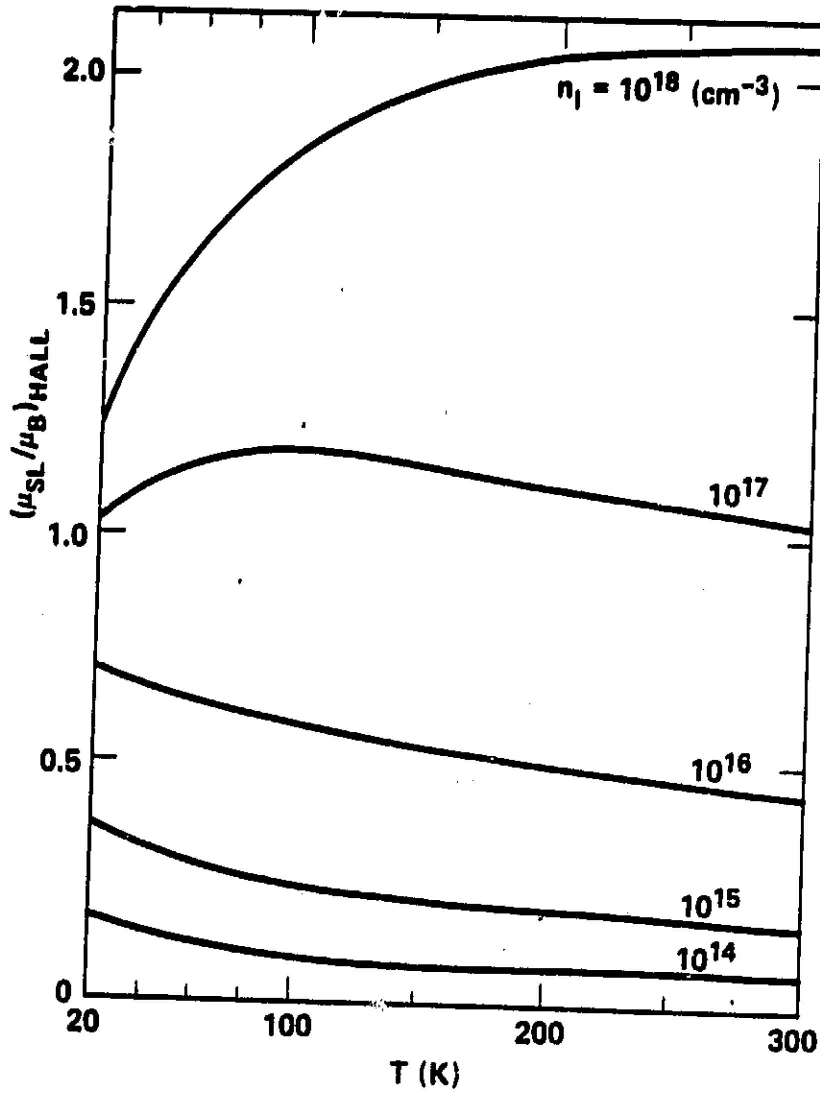

Fig. 22. Variation of the impurity-scattering-limited electron Hall mobility with temperature T for various donor concentrations, as in Fig. 21.

V. THIN METAL LINE FABRICATION

We have made a reasonably thorough literature search of recent developments in fine-line technology and have uncovered a wide range of techniques all of which can basically be catagorized as either X-ray, electron-beam, ion-beam, or optical lithographies. In our laboratory, only optical lithography was available, and the most promising optical method we discovered was one reported by Speidell[27] at IBM. He claimed lines as narrow as 600 A with his technique, and, as a preliminary test, we decided to try it in our lab. We closely followed his procedure, modifying steps only according to the facilities available to us. The complete procedure and results are described as follows.

On several clean silicon wafers, oxides of thickness ≈ 3400 A were grown. Standard clean 1 (SC1) was prepared as a 7:3:3 solution by volume of deionized (DI) water, H_2O_2 (30%), and NH_4OH (29%). This solution was used at about 80°C for 20 minutes to clean the oxidized wafers. Next the wafers were prebaked at 180°C for 30 minutes, coated with hexamethyldisilazane at 4000 rpm for 15 seconds, then coated with AZ 1350J photoresist at 5000 rpm for 20 seconds, and finally baked at 65°C for 25 minutes. Since we desired an undercut in the photoresist layers, the soft-baked wafers were next soaked for 5 minutes in chlorobenzene and soft-baked again for 30 minutes at 65°C.

With a previously-prepared mask for 2.5 μm lines, the wafers were UV exposed for 15 seconds. We used high-speed developer (1:3.5 of AZ developer and water) to develop the wafers. They were developed for 9 sec with 3 minutes of DI rinse, then placed in the developer for 1 minute and rinsed in running DI water for 3 minutes. The dried wafers were hard-baked for 30 minutes at 125°C in vacuum.

Figure 23 shows SEM photos of typical photoresist structures we so achieved. Because of the chlorobenzene soak, undercuts or "lips" are clearly visible on either side of the line. These "lips" are less than 1/3 of the total thickness of the line. We estimate that each undercut is approximately 4000 A wide. The size of the undercut can be reduced by reducing the soaking time in chlorobenzene. The undercut is made at a rate of approximately 800 A per minute of soaking time in chlorobenzene.

The desired thin metal lines are achieved by evaporating Al at an angle of 20° into the undercuts. To etch away the unwanted Al and photoresist, we tried two different methods. First, the wafers were heated in acetone for 5 minutes and cleaned in an ultrasonic cleaner for 1 minute. The photoresist surface is thereby removed without disturbing the Al. Then an etch was done to remove Al layers between the two lines that are formed in the two undercuts. The etch removed Al between the

lines but also smeared out the two lines at the same time. To get sharper lines, we followed the reverse procedure. That is, we first did the Al etching and then removed the photoresist. The latter gave reasonably sharp Al lines.

The final line thickness we achieved was ≈ 4000 A, dictated by the size of the undercuts. This dimension can definitely be reduced to the the order of 600 A, as demonstrated by Speidell[27], by appropriately reducing the soak time in chlororbenzene. To obtain even thinner lines, on the order of 100-200 A, however, will undoubtedly require X-ray or electron-beam lithographies. For this reason and because we had no immediate scheme in mind to produce the periodic line pattern (Fig. 1) required for an MOS superlattice, we did not pursue this study further.

ORIGINAL PAGE
BLACK AND WHITE PHOTOGRAPH

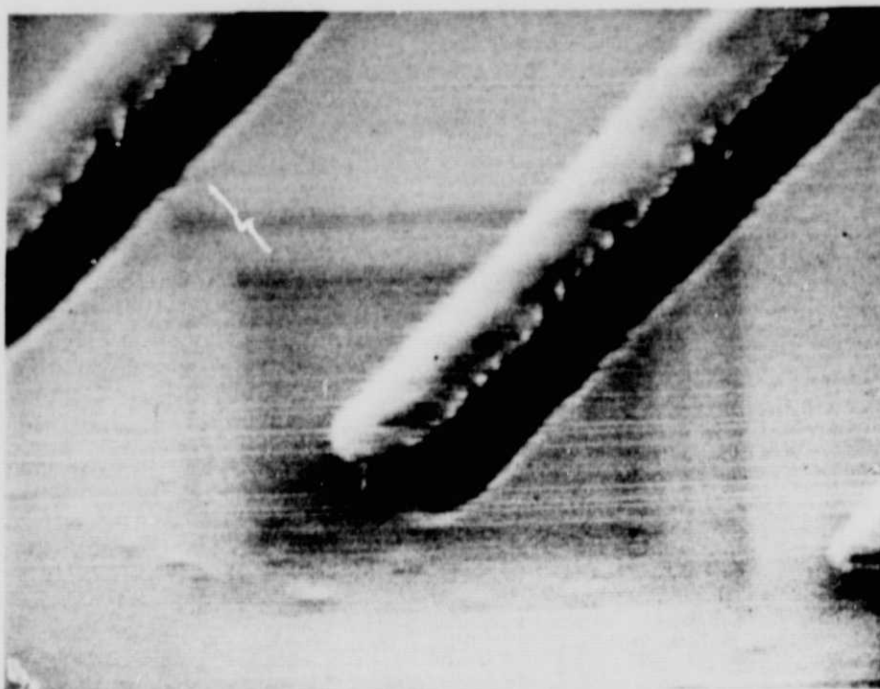

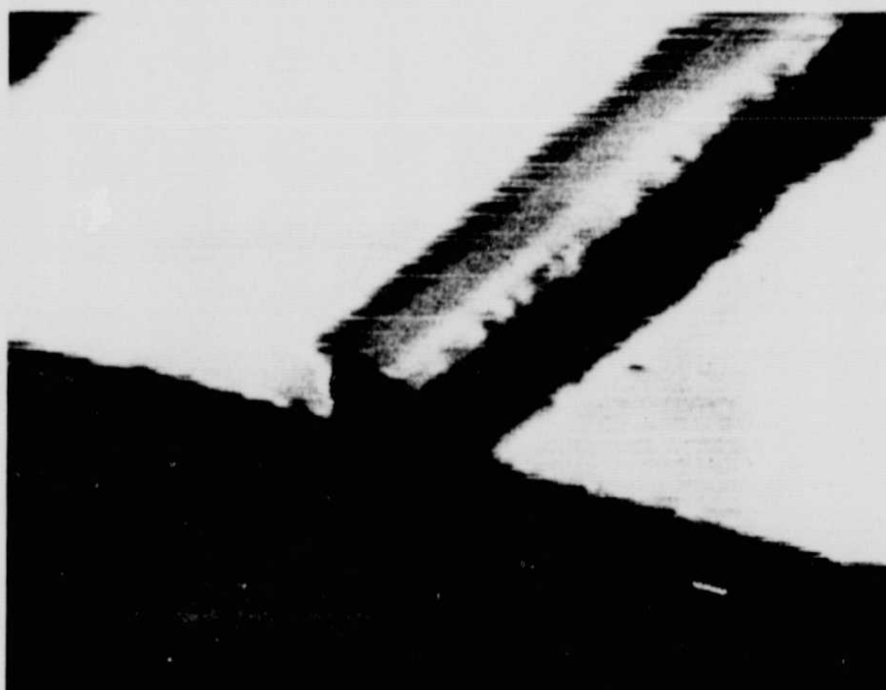

Fig. 23. Photoresist strucuture used to fabricate thin Al metal lines in our laboratory, as described in the text. Top panel: 10,000x magnification; bottom panel: 7,000x magnification.

VI. CONCLUSIONS

Our results bode well for the propspect of achieving enhanced electron mobilities in silicon superlattice systems. We have seen that the general trends in band structure indicate a reduced electron conductivity effective mass in the transverse direction, with a unique symmetry lowering in [100]-oriented superlattices playing a leading role. For a fixed superlattice potential strength, this effect initially increases with layer thickness, but quickly saturates to a limiting value. Phonon-scattering-limited mobility, which is dominant at room temperature, should be most strongly enhanced by this mechanism, with an ideal limiting enhancement of 2.20 predicted if all other things are equal. The two-dimensional nature of the transport, however, also brings with it a strong dependence of mobility on carrier concentration. Our calculations show that impurity-scattering-limited mobility, which is dominant at low temperatures, will actually be diminished at low carrier concentrations and enhanced only for high carrier concentrations.

Since our band-structure model for silicon superlattices is an idealization we expect that any mobility calculated on the basis of our model should represent an approximate upper limit for given geometrical conditions. Two principal effects which need to be addressed more thoroughly in any refined theoretical treatment are (i) chemical disorder in the $Si_{1-x}Ge_x$ layer of the superlattice in the type-II case and (ii) surface effects, including band-bending, strain fields, and possible defects at the interfaces between layers. Physically, both of these effects should decrease any measured electron mobility. In addition, interband scattering, which was neglected in our impurity-scattering-limited mobility calculation should also decrease the actual mobility.

The most pressing need for the near term, however, is some hard experimental data on high-quality superlattice structures. Hopefully, this will be forthcoming in the Si-$Si_{1-x}Ge_x$ case with the new work initiated at Bell Laboratories.[9] Also, the fabrication of an MOS superlattice should be given some serious consideration in light of the continuing rapid developments in fine-line technology.

VII. CONFERENCE PAPERS AND PUBLICATIONS

Below is a summary of all written and oral output connected with this research:

(a) Contributed conference papers:

1. "Theory of Silicon Superlattices," J. A. Moriarty, Bull. Am. Phys. Soc. 26, 421 (1981).

2. "Electronic Structure of Silicon Superlattice Systems," S. Krishnamurthy and J. A. Moriarty, Bull. Am. Phys. Soc. 29, 215 (1984).

3. "Electronic Structure of Silicon Superlattices," S. Krishnamurthy and J. A. Moriarty, Superlattices and Microstructures (in press).

(b) Journal publications:

1. "Theory of Silicon Superlattices: Electronic Structure and Enhanced Mobility," J. A. Moriarty and S. Krishnamurthy, J. Appl. Phys. 54, 1892 (1983).

2. "Electronic Structure and Impurity-Limited Electron Mobility of Silicon Superlattices," S. Krishnamurthy and J. A. Moriarty, Phys. Rev. B (to be published).

(c) Theses:

1. "The Theory of Silicon Superlattices: Band Structure and Mobility Enhancement," S. Krishnamurthy, Ph. D. thesis (University of Cincinnati, 1984) (unpublished).

REFERENCES

1. L. Esaki and R. Tsu, IBM J. Res. Dev. 14, 61 (1970).
2. L. Esaki and L. L. Chang, Crit. Rev. Solid State Sci. 6, 195 (1976) and references therein.
3. J. A. Moriarty and S. Krishnamurthy, J. Appl. Phys. 54, 1892 (1983).
4. S. Krishnamurthy, Ph. D. thesis (University of Cincinnati, 1984) (unpublished).
5. S. Krishnamurthy and J. A. Moriarty, Phys. Rev. B (to be published).
6. H. M. Manasevit, I. S. Gergis, and A. B. Jones, Appl. Phys. Lett. 41, 464 (1982); A. B. Jones (private communication).
7. R. Dingle, H. L. Stromer, A. C. Gossard, and W. Wiegmann, Appl. Phys. Lett. 33, 665 (1978).
8. G. C. Osbourn, Phys. Rev. B 27, 5126 (1983).
9. A. T. Fiory, Bull. Am. Phys. Soc. 29, 499 (1984) and private communication.
10. P. J. Stiles, Surf. Sci. 73, 252 (1978).
11. G. H. Dohler, Phys. Status Solidi B 52, 79 (1972) and 52, 533 (1972).
12. K. Ploog, A. Fisher, and H. Kunzel, J. Electrochem. Soc. : Solid-State Science and Technology 128, 400 (1981).
13. G. H. Dohler, H. Kunzel, D. Olego, K. Ploog, P. Ruden, H. J. Stolz, and G. Abstreiter, Phys. Rev. Lett. 47, 864 (1981).
14. T. J. Drummond, H. Morkoc, and A. Y. Cho, J. Appl. Phys. 52, 1380 (1981).
15. K. Hess, Appl. Phys. Lett. 35, 484 (1979).
16. S. M. Sze, *Physics of Semiconductor Devices* (Wiley, New York, 1969).
17. W.A. Harrison, *Electronic Structure and the Properties of Solids*, (Freeman, San Francisco, 1980).
18. D. J. Chadi and M. L. Cohen, Phys. Status Solidi B 68, 405 (1975).
19. J. R. Chelikowsky and M. L. Cohen, Phys. Rev. B 14, 556 (1976).
20. A. G. Milnes and D. L. Feucht, *Heterojunctions and Metal-Semiconductor Junctions* (Academic, New York, 1972).
21. G. Margaritondo, A. D. Katnami, N. G. Stoffel, R. R. Daniels, and Te-Xiu Zhao, Solid State Commun. 43, 163 (1982); G. Margaritondo, N. G. Stoffel, and A. D. Katnami, Solid State Commun. 36, 215 (1980).
22. J. N. Schulman and Y. C. Chang, Phys. Rev. B 24, 4445 (1981).
23. V. Heine, Proc. Phys. Soc. London 81, 300 (1963).
24. Y. C. Chang, Phys. Rev. B 25, 605 (1982) and Y. C. Chang and J. N. Schulman, Phys. Rev. B 25, 3975 (1982).
25. S. Mori and T. Ando, J. Phys. Soc. Jap. 48, 865 (1980).
26. R. A. Smith, *Semiconductors* (Cambridge, New York, 1978).
27. J. L. Speidell, J. Vac. Sci. Tech. 19, 693 (1981).